

Testing velocity kinks as a planet-detection method: Do velocity kinks in surface gas emission trace planetary spiral wakes in the midplane continuum?

JESSICA SPEEDIE ¹ AND RUOBING DONG ^{1,2}

¹*Department of Physics & Astronomy, University of Victoria, Victoria, BC, V8P 1A1, Canada*

²*Kavli Institute for Astronomy and Astrophysics, Peking University, Beijing 100871, China*

(Received 2022 September 20; Accepted 2022 November 1)

Submitted to ApJL

ABSTRACT

Spiral density waves generated by an embedded planet are understood to cause “kinks” in observed velocity channel maps of CO surface emission, by perturbing the gas motion within the spiral arms. If velocity kinks are a reliable probe of embedded planets, we should expect to see the planet-driven spiral arms in other observational tracers. We test this prediction by searching the dust continuum for the midplane counterparts of the spirals responsible for all of the velocity kink planet candidates reported to date, whose orbits lie inside the dust continuum disk. We find no clear detection of any spiral structure in current continuum observations for 6 of the 10 velocity kink planet candidates in our sample (DoAr 25, GW Lup, Sz 129, HD 163296 #2, P94, and HD 143006), despite the high planet masses inferred from the kink amplitude. The remaining 4 cases include 3 clear detections of two-armed dust spirals (Elias 27, IM Lup and WaOph 6) wherein neither spiral arm aligns with a wake originating from reported planet location, suggesting that under the planetary-origin hypothesis, an accurate method for inferring the location of the planet in the midplane may need to encompass vertical effects. The 10th case, HD 97048, is inconclusive with current knowledge of the disk geometry.

Keywords: Planetary-disk interactions (2204), Exoplanet detection methods (489), Protoplanetary disks (1300), Planet formation (1241), Exoplanet formation (492)

1. INTRODUCTION

The velocity “kink” kinematic signature has gained standing as a promising method for discovering embedded planets (Disk Dynamics Collaboration et al. 2020; Pinte et al. 2022). To date, 12 planet candidates have been reported based on velocity kink detections; in three cases, the planets have been ingested into the NASA or European exoplanet databases as *confirmed* planets¹ (Pinte et al. 2019; Izquierdo et al. 2022), and in one case, the candidate’s circumplanetary disk has been observed co-located with the kink (AS 209, Bae et al. 2022). Many more such detections of embedded planets are expected with the upcoming exoALMA Large Program².

Some loose ends exist, however, that motivate independent verification of the planetary origin of velocity

kinks. Eleven of the 12 velocity kink detections were made in ¹²CO emission, which is expected to originate above the midplane (e.g., Law et al. 2021), outside of where any analytic theory of velocity kinks has been achieved (Bollati et al. 2021). Ten of the 12 detections were made by visual inspection, without an assessment of the statistical significance of the kink signal (Pinte et al. 2018a, 2019, 2020), and in some cases the detections do not appear in independent datasets (Teague et al. 2021b). While the planet hypothesis is on the one hand supported by the inferred planet locations coinciding with dust gaps, the mass needed to generate kinks with the observed amplitudes is higher than the planet mass derived from the properties of the dust gaps by a factor of 4 – 100 (e.g., Lodato et al. 2019; Zhang et al. 2018).

The velocity kink signal is understood to be generated by the embedded planet’s spiral wakes. Along the spiral arms, the gas motion is perturbed relative to Keplerian rotation, which appears as an excess and absence of emission (i.e., a “kink”) in the channel maps (e.g., Bollati et al. 2021). This understanding en-

Corresponding author: JS, RD
jspeedie@uvic.ca, rbdong@uvic.ca

¹ HD 97048 b; HD 163296 b; HD 163296 c (links embedded).

² 2021.1.01123.L; <https://www.exoalma.com/>

ables us to make a robust, testable prediction: *All instances of planet-driven velocity kinks should be concurrent with planet-driven spiral arms.* Recently, [Calcino et al. \(2022\)](#) demonstrated that the velocity kinks observed in ^{12}CO emission in HD 163296 map directly onto the theoretical curve for the spiral wake driven by planet c, projected up onto the emission surface. In this letter, we search the disk midplane for the spiral arms driven by 10 velocity kink planet candidates, using (sub-)mm continuum observations, under the usual assumption that the \sim (sub)-mm-sized dust traced by such observations has settled to the disk midplane. Our goal is to provide an independent verification for the existence of the predicted planets, and thereby test the validity of velocity kinks as signposts of planets in disks.

2. DATA & METHODS

2.1. Sample: Disks with Velocity Kinks

We compile all the disks with velocity kinks reported in the literature to date:

- 1 kink in HD 163296 (“HD 163296 #1”) from [Pinte et al. \(2018a\)](#) (hereafter [Pin18](#))
- 1 kink in HD 97048 from [Pinte et al. \(2019\)](#) (hereafter [Pin19](#))
- 9 kinks (8 new) in 8 DSHARP disks: Elias 27, HD 143006, HD 163296 (a second kink in this disk: “HD 163296 #2”), IM Lup, DoAr 25, GW Lup, Sz 129 and WaOph 6, from [Pinte et al. \(2020\)](#) (hereafter [Pin20](#))
- 2 kinks in HD 163296 (a third unique kink, “P94”, and an independent re-detection of HD 163296 #1, dubbed “P261”) from [Izquierdo et al. \(2022\)](#) (hereafter [Izq22](#))
- and 1 kink in AS 209 co-located with a CPD candidate from [Bae et al. \(2022\)](#) (hereafter [Bae22](#)).

In total, 12 velocity kinks have been reported in 10 disks. With the exception of P261 and P94 in HD 163296 (which were identified by `discminer`; [Izq22](#)), all the detections have been made by visual inspection of the channel maps, and the statistical significance of the detections has not been quantified. We list the disks and relevant properties of the kink detections in Table 1.

We then exclude from our sample the detections with inferred planet locations exterior to the outer edge of continuum emission. This eliminates HD 163296 #1 a.k.a P261 ([Pin18](#); [Izq22](#)) and AS 209 ([Bae22](#)), leaving us with a total of 10 velocity kinks in 9 disks (where the repeat disk is HD 163296 containing [Pin20](#)’s HD 163296 #2 kink and [Izq22](#)’s P94 kink).

As a side note, velocity deviations attributed to a planet have also been reported in HD 100546 ([Casassus & Pérez 2019](#); [Pérez et al. 2020](#)) and TW Hya ([Teague](#)

[et al. 2022](#)). We do not consider these detections in this work primarily³ because we are concerned with detections based on kinks in velocity channel maps, whereas these were made based on Doppler flips in velocity residual maps.

Planet location. The works reporting the velocity kinks in our sample provide the midplane location of the predicted planets. As we are testing this prediction, we adopt the given locations. For 9 of our 10 candidate planets (the exception being P94 in HD 163296; [Izq22](#)), the procedure that was used to determine the planet location is the following ([Pin19](#); [Pin20](#)):

- i) Identify the CO channel in which the velocity kink is most prominently detected, by visual inspection;
- ii) Identify the center of the kink in that channel, by visual inspection;
- iii) Measure the altitude of the CO emission surface at the center of the kink, using the method of [Pinte et al. \(2018b\)](#);
- iv) Deproject that location onto the disk midplane.

In these 9 cases, the planet position is given in sky-coordinates (r_p , PA_p) without an estimate of spatial uncertainty.

The location of the P94 planet in HD 163296 is retrieved by `discminer`,⁴ in disk-frame coordinates (R_p , ϕ_p), with an uncertainty in the radial and azimuthal directions of ± 6 au and ± 3 degrees, respectively ([Izq22](#)). However, due to `discminer`’s velocity centroid folding procedure,⁵ the retrieved polar angle is degenerate about the disk minor axis and additional information or reasoning is needed to subsequently determine if the detection is on the redshifted or blueshifted side of the disk. The `discminer` velocity residuals of P94 were found to have a Doppler flip morphology, and by reasoning that the sub-Keplerian branch should be interior to

³ Additionally, the HD 100546 planet lies inside a continuum ring ($0.01 \pm 0.04''$, $0.21 \pm 0.04''$ on the sky; [Casassus & Pérez 2019](#)), which is contrary to the classical paradigm that embedded planets carve gaps (though would support the scenario of [Nayakshin et al. 2020](#)). Since the initial discovery, the velocity deviations in HD 100546 have been explained as being due to an inner binary companion ([Norfolk et al. 2022](#)), and due to disk eruptions driven by an embedded outflow ([Casassus et al. 2022](#)). The inferred planet location in TW Hya ($r_p = 1.53''$ or 82 au, $\text{PA}_p = 60^\circ$) lies outside of the outer edge of continuum emission that is detected when observed at high angular resolution (~ 30 mas, [Huang et al. 2018a](#)), and the existing observations with sufficient sensitivity to detect continuum emission extending beyond 82 au are too low angular resolution for our purposes ($0.37''$, [Ilee et al. 2022](#)).

⁴ We note that `discminer` assesses the significance of a deviation from Keplerian velocity, not whether the deviation matches the expected morphology of a planet-driven velocity deviation (as this has not yet been described analytically in 3 dimensions).

⁵ A way of removing contributions to the velocity field that are symmetric about the disk minor axis, stemming from gas gaps and bulk disk rotation.

the planet’s orbit and the super-Keplerian branch should be exterior (Bollati et al. 2021), Izo22 report the planet on the redshifted side. We note that the “mirror kink” (i.e., the detection with opposite sign but equal significance, on the blueshifted side) is co-located with Pin20’s HD 163296 #2 kink (Footnote 11, Izo22).

We list the reported locations of the candidate planets in our sample in Table A1. In all cases, the inferred location pinpoints the planet within a dust gap.

2.2. Dataset: Continuum Observations

The continuum data we present in this Letter are from the same ALMA program as the CO data in which the velocity kinks were detected. For the 8 Pin20 disks, we retrieve the publicly available, self-calibrated science-ready continuum images and fiducial (continuum-subtracted) $^{12}\text{CO } J = 2 - 1$ image cubes from the DSHARP data repository.⁶ For HD 97048, we obtain the self-calibrated continuum images and $^{13}\text{CO } J = 3 - 2$ cube from Figshare.⁷ Our analysis is only focused on the continuum images, and we do no new analysis on the CO cubes. Table A2 summarizes the observations and some basic properties of the data. For observational setup and data reduction details, we refer the reader to Pin19 for HD 97048, and to Andrews et al. (2018) for the 8 DSHARP disks in our sample. We measure the rms noise in the continuum images inside an annulus centered on the disk whose outer radius is the maximum allowed by the field of view and inner radius sufficiently larger than the source, following Andrews et al. (2018). For reference, we also measure the rms noise in the CO cubes, in the same annular area, throughout the first and last 5 channels.

2.3. Methods: Searching for Dust Spirals

Approach. Since spirals are perturbations in surface brightness above/below the background disk, our approach is to subtract an axisymmetric model for the background in order to extract the spiral signal. We create this axisymmetric background model in the image plane, by azimuthally averaging the continuum image.

We choose to do our analysis in the image plane, rather than the visibility domain, for two main reasons. Firstly, it yields similar results to uv -plane fitting in terms of both the morphology and sensitivity of the residuals, and is easily reproducible. We discuss this in more detail in Appendix §D.1. Secondly, the disk conditions (equation of state, optical depth, planet mass) and observing setups (angular resolution, sensitivity) under which the image plane method successfully retrieves the spiral signal has been quantified on synthetic continuum observations of planet-driven dust spirals in hydrodynamic simulations (Speedie et al. 2022). We therefore

can form apples-to-apples expectations for the observability of the dust spirals, which we describe in detail in §2.4.

Disk geometry. Knowledge of the inclination and position angle of the continuum disk is needed to create the axisymmetric background model, and Table A3 provides the geometrical parameters we use for each disk. For 4 of the 8 DSHARP disks (HD 143006, HD 163296, GW Lup and Sz 129), we use the values found in Andrews et al. (2021) (their Table 2) by the frank (Jennings et al. 2020) residual appearance method. We also tried the Huang et al. (2018b) geometries for these 4 disks and found that it had no effect on our results. For the other 4 not in Andrews et al. (2021) (Elias 27, IM Lup, DoAr 25 and WaOph 6), we use the values found in Huang et al. (2018b) (their Table 2) by fitting ellipses to individual annular dust substructures. For HD 97048, no continuum-derived geometry has been published to our knowledge. We thus adopt two possible geometries, found by different methods: (i) fitting a Keplerian disk model to the velocity field from CO line data cubes (Table C.1, Bohn et al. 2022) using eddy (Teague 2019a); (ii) fitting ellipses to rings and gaps in near-IR scattered light (Table 1, Ginski et al. 2016).

Disk rotation direction. We assume the predicted planet orbits in the same direction that the disk rotates. For HD 163296, DoAr 25 and HD 97048, it has been determined which side of the disk major axis is the near/far side with existing scattered light observations (see notes for Col. 10 in Table A3 for references), and we use that information in conjunction with knowing which side about the minor axis is the blue/redshifted side to deduce the direction that the disk rotates. For HD 143006 and GW Lup (low inclination disks), the near/far side determination not definitive (e.g., Benisty et al. 2018), but Pérez et al. (2018) suggest HD 143006’s west side is the near side, and Garufi et al. (2022) posit GW Lup’s northwest side is mostly likely the near side. This would mean HD 143006 rotates clockwise and GW Lup rotates anti-clockwise. In the former case this happens to be the opposite direction to the “low-level” tentative large-scale Archimedean spiral found by Andrews et al. (2021) (see Appendix §D.1 for more discussion). For Sz 129, a relatively unstudied disk, no scattered light observations exist in the literature to our knowledge. Our results (Figs. 1 & 2) will show that the rotation direction of these 3 disks –HD 143006, GW Lup and Sz 129– is rendered irrelevant by the lack of spiral features in their continuum residual maps, but we still wish to show the tightness of the spiral winding. For that purpose, we assign clockwise for HD 143006 and anti-clockwise for GW Lup (motivated by the suggestions of Pérez et al. 2018; Garufi et al. 2022) and anti-clockwise Sz 129 (arbitrarily). For Elias 27, IM Lup and WaOph 6, we adopt the rotation direction found in Huang et al. (2018c) (their §3.2).

⁶ <https://almascience.eso.org/almadata/lp/DSHARP/>

⁷ DOI: <https://doi.org/10.6084/m9.figshare.8266988.v1>

Table 1. Sample and summary of possibly planet-induced velocity kink detections to date.

Disk	Ref.	Method	Line	v_{res} (m/s)	$v_{\text{kink channel}}$ (km/s)	Δv	σ_{kink}	S/N _{CO}	Gap	M_{p} (M_{Jup})	Notes
(1)	(2)	(3)	(4)	(5)	(6)	(7)	(8)	(9)	(10)	(11)	(12)
Kinks inside the continuum emission disk											
Elias 27	Pin20	VI	¹² CO(2−1)	350	1.70	“?”	Firm	12	D69	1−3	<i>a</i>
HD 143006	Pin20	VI	¹² CO(2−1)	320	8.84	$\approx 0.2 v_{\text{Kep}}$	Firm	10	D22	1−3	<i>g</i>
HD 163296 (P94)	Izq22	discminer	¹² CO(2−1)	320	6.28	0.41 km/s	(19.4, 7.5)	...	D86	1−3	<i>b</i>
HD 163296 (#2)	Pin20	VI	¹² CO(2−1)	320	3.40	$\approx 0.15 v_{\text{Kep}}$	Firm	36	D86	1−3	<i>b, f</i>
IM Lup	Pin20	VI	¹² CO(2−1)	350	3.05	$< 0.24 v_{\text{Kep}}$	Firm	14	D117	1−3	<i>c</i>
DoAr 25	Pin20	VI	¹² CO(2−1)	350	5.05	“?”	Tent.	7	D98	1−3	<i>a</i>
GW Lup	Pin20	VI	¹² CO(2−1)	350	2.70	$< 0.3 v_{\text{Kep}}$	Tent.	12	D74	1−3	
Sz 129	Pin20	VI	¹² CO(2−1)	350	4.80	$< 0.2 v_{\text{Kep}}$	Tent.	11	D64	1−3	
WaOph 6	Pin20	VI	¹² CO(2−1)	350	2.10	“?”	Tent.	13	D79	1−3	<i>a</i>
HD 97048	Pin19	VI	¹³ CO(3−2)	120	5.76	130 au	2−3	
Kinks outside the continuum emission disk											
HD 163296 (#1, P261)	Pin18	VI & discminer	¹² CO(2−1)	110	1.00	0.40 km/s	(5.2, 4.6) ^d	...	N/A	2	<i>d, e</i>
AS 209	Bae22	VI	¹² CO(2−1)	200	4.80	N/A	$1.3 \cdot (\alpha/10^{-3})^{1/2}$	

NOTE—The last two rows are not in our sample, as the inferred planet location lies outside the continuum emission disk, but we include them for completeness. Column descriptions:

- (1) Name of disk. Name of kink or planet candidate in brackets, if applicable.
- (2) Paper first reporting the velocity kink. All values in the corresponding row are from this reference unless otherwise noted.
- (3) Method by which the velocity kink was detected. “VI” means visual inspection of the channel maps, and discminer is the quantitative tool of Izquierdo et al. (2021).
- (4) CO isotopologue and J transition in which the kink is reported.
- (5) Velocity (spectral) resolution of the CO cube in which the kink is reported.
- (6) Velocity (relative to Earth) of the channel in which the kink is most prominently detected, which is used to pinpoint the planet location (see Sec. 2.1). The two exceptions to this are: (i) Izq22 (row 3): the value in this entry is one of two channels in which the authors note the kink can be seen visually (caption of their Fig. 1), and discminer is used to pinpoint the planet location; (ii) Bae22 (row 12): the value in this entry is the channel in which the CPD candidate is most clearly detected in ¹³CO, and is the central of three channels in which the ¹²CO velocity kink is reported.
- (7) Amplitude of the velocity deviation. “?” is verbatim from the reporting paper, and ‘.’ means not provided by the authors. For an independent velocity deviation prediction from 3D simulations for some of the DSHARP disks, see Rabago & Zhu (2021).
- (8) Either a qualitative classification as a “firm” or “tentative” kink detection by Pin20, or, the statistical significance (σ_r, σ_ϕ) of the deviation from Keplerian velocity from discminer (Izq22).
- (9) Signal to noise of CO emission at the location of the kink.
- (10) Dust gap associated with inferred planet location. Gap name designation from Huang et al. (2018b) for the DSHARP disks, and approximate gap radius in au for HD 97048 (Pin19).
- (11) Mass estimate of the candidate planet, inferred from the velocity kink amplitude. For the Pin18, Pin19 and Pin20 disks, this is from forward modeling with SPH simulations; for P94 it is from forward modeling with hydrodynamic simulations (Izq22); and for AS 209 (Bae22) it is from the Kanagawa et al. (2016) empirical relation between the gas gap width and planet mass. For mass estimates derived from the dust gap properties, see Zhang et al. (2018) and Lodato et al. (2019).
- (12) Notes:
 - (a) Channel maps suffer from cloud contamination (Column 7, Table 5, Andrews et al. 2018). Visually, the affected velocities are: 2.75 − 4.85 km/s (7 channels) for Elias 27; 1.55 − 5.05 km/s (11 channels) for DoAr 25, and 2.45 − 4.20 km/s (6 channels) for WaOph 6.
 - (g) Simulation work supporting the existence of this planet: Ballabio et al. (2021).
 - (b) The HD 163296 #2 and P94 kinks have the same polar angle, if mirrored about the disk minor axis (Footnote 11, Izq22).
 - (c) Simulation work supporting the existence of a planet in this disk; mirrored about the disk minor axis (Footnote 11, Izq22).
 - (d) Value of σ_{kink} in this row is from Izq22 with discminer.
 - (e) Simulation work supporting the existence of this planet: Calcino et al. (2022).
 - (f) Not verified in ¹²CO channel maps from the MAFS program (Teague et al. 2021b).

2.4. Expectations: Dust Spirals Driven by the Velocity Kink Planets

Midplane spiral morphology. We expect the embedded planets predicted by the velocity kink detections to drive spiral wakes in the gas at the midplane whose intrinsic morphology (amplitude, width and phase) is determined by the planet mass and location, as well as disk temperature.

As we are searching for these spirals in the (sub-)mm continuum and not the gas, the first question is whether we expect a difference between the dust spiral morphology and the morphology of the spiral in the gas. This depends on how quickly the dust responds to the change in aerodynamic drag forces exerted by the gas when the grains encounter the gas spiral perturbation, which in turn depends on the dust grain size and the local gas surface density. [Sturm et al. \(2020\)](#) and [Speedie et al. \(2022\)](#) showed that for dust with Stokes number ($St \propto a_{\text{grain}} \Sigma_{\text{gas}}^{-1}$, where a_{grain} is the dust grain size and Σ_{gas} is the local gas surface density) lower than the critical Stokes number, $St \lesssim St_{\text{crit}} \approx 0.05 - 0.1$,⁸ the dust responds quickly enough such that the resulting dust spiral is morphologically identical to the driving gas spiral at the midplane. We expect our continuum observations to be most sensitive to thermal emission from dust grains of size $a_{\text{grain}} \approx \lambda_{\text{obs}}/2\pi$ ([Kataoka et al. 2015](#); [Pavlyuchenkov et al. 2019](#)), which translates to $a_{\text{grain}} \approx 0.14$ mm for HD 97048 (Band 7) and $a_{\text{grain}} \approx 0.20$ mm for the 8 DSHARP disks (Band 6). For gas surface densities higher than just $\sim 0.2 \text{ g cm}^{-2}$, these grain sizes correspond to Stokes numbers lower than St_{crit} (see Fig. 2 of [Speedie et al. 2022](#)). Figure 7 of [Dullemond et al. \(2018\)](#) shows inferred gas surface densities for a subset of the DSHARP disks (including 3 in our sample) to range $0.1 \lesssim \Sigma_{\text{gas}} \lesssim 50 \text{ g cm}^{-2}$. To put it another way, assuming a gas surface density profile $\Sigma_{\text{gas}} \sim 1/r$, then in order for Σ_{gas} to be lower than 0.2 g cm^{-2} at 50 au (typical location of inner arms in our sample), the total disk mass contained within 100 au would need to be lower than $6.7 \times 10^{-4} M_{\odot}$. We therefore expect no difference between the intrinsic morphology of the predicted midplane gas spiral and that of the dust spiral we aim to observe, and can use the literature knowledge of gas spirals to understand the morphology of the expected dust spirals.

The trajectory of a planet-driven spiral (i.e., the azimuthal location of the spine, or peak amplitude, as a function of radius) is the result of constructive interference among various spiral wave modes, each excited by a different Fourier component of the planet’s gravitational

potential ([Bae & Zhu 2018a,b](#)). To predict where we expect to see positive residuals (emission above the axisymmetric background) in the continuum residual map for each planet in our sample, we use the analytic phase equation of [Bae & Zhu \(2018a\)](#):⁹

$$\phi_{m,n}(R) = -\phi_{\text{p}} - \text{sgn}(R - R_{\text{p}}) \frac{\pi}{4m} + 2\pi \frac{n}{m} - \int_{R_{\text{m}}^{\pm}}^R \frac{\Omega(R')}{c_{\text{s}}(R')} \left| \left(1 - \frac{R'^{3/2}}{R_{\text{p}}^{3/2}} \right)^2 - \frac{1}{m^2} \right|^{1/2} dR', \quad (1)$$

where $(R_{\text{p}}, \phi_{\text{p}})$ are the midplane coordinates of the planet in the disk frame, $\Omega(R)$ is the angular velocity of the disk, $c_{\text{s}}(R)$ is the sound speed of the gas, and m is the azimuthal wavenumber of the wave mode excited by the m th Fourier component of the planet’s potential, which itself has a number of components indexed by n . The $n = 0$ components form the primary spiral arms, which are easier to recognize than e.g. secondary arms ($n = 1$ for $R < R_{\text{p}}$, or $n = m - 1$ for $R > R_{\text{p}}$) because: (i) they are launched relatively near to the planet, at Lindblad resonances $R_{\text{m}}^{\pm} = (1 \pm 1/m)^{2/3} R_{\text{p}}$ ([Goldreich & Tremaine 1979](#)), and therefore the inner and outer primary arms always “point” to the planet, whereas the location of the additional arms (both the starting point and the azimuthal separation from the primary) varies with planet mass ([Fung & Dong 2015](#)); and (ii) close to the planet, they have the highest amplitude ([Bae & Zhu 2018a](#)). As such, we set $n = 0$.

The third term in Eqn. 1 is the only radially-varying term, and describes how tightly wound the spiral wave modes are as they propagate away from the planet. In addition to m , this term depends on the gas pressure scale height, $H(R) = c_{\text{s}}/\Omega$. We calculate $\Omega(R)$ as the Keplerian angular velocity $\Omega(R) = (GM_{\star}/R^3)^{1/2}$, where R is the disk-frame radial coordinate and M_{\star} is the stellar mass (Col. 3, Table A3). We calculate the gas sound speed as

$$c_{\text{s}}(R) = \left(\frac{k_{\text{B}} T_{\text{d}}(R)}{\mu m_{\text{prot}}} \right)^{1/2}, \quad (2)$$

where k_{B} is the Boltzmann constant, $\mu = 2.37$ is the mean molecular weight of the gas in atomic units, and m_{prot} is the proton mass. We thus need an analytic estimate for the disk temperature at the midplane $T_{\text{d}}(R)$, for which we use the simple irradiated flaring disk recipe of [Dullemond et al. \(2018\)](#):

$$T_{\text{d}}(R) = \left(\frac{\frac{1}{2} \varphi L_{\star}}{4\pi r^2 \sigma_{\text{SB}}} \right)^{1/4}. \quad (3)$$

⁸ The critical Stokes number is the Stokes number for which the time it takes a dust grain to cross the spiral wake is equal to the grain’s stopping time, and so this range is introduced by the azimuthal width of the wake, which changes with planet mass and distance from the planet (§3.2, [Speedie et al. 2022](#)).

⁹ This equation assumes a circular orbit for the planet; see [Zhu & Zhang \(2022\)](#) and [Fairbairn & Rafikov \(2022\)](#) for semi-analytic linear theory of spiral density waves excited by planets on eccentric orbits.

Here, L_* is the luminosity of the central star (Col. 4, Table A3), σ_{SB} is the Stefan-Boltzmann constant and φ is the flaring angle (e.g., Chiang & Goldreich 1997; Dullemond et al. 2001). A smaller flaring angle corresponds to a colder temperature profile and a more tightly wound spiral. We assign $\varphi = 0.02$ to be consistent with Dullemond et al. (2018) and Huang et al. (2018b).

Returning to the m dependence of the third term in Eqn. 1, we expect the phase of the spiral we see to follow that of the dominant azimuthal mode, $m_{\text{dom}} = (\frac{1}{2})(H/r)_{\text{p}}^{-1}$, in the case of low mass planets ($M_{\text{p}} \lesssim 0.1 M_{\text{th}}$, where $M_{\text{th}} = c_s/\Omega G = (H/r)_{\text{p}}^3 M_*$ is the unit of thermal mass; Bae & Zhu 2018a,b). However, for higher mass planets, the wave modes propagate at faster speeds, and the resulting spiral arms are more open (Goodman & Rafikov 2001) and should more closely follow lower ($m < m_{\text{dom}}$) modes. In Col. 8 of Table A1, we convert the predicted masses of the embedded planets (1–3 M_{Jup} , Col. 8 of Table 1) into units of M_{th} using our estimation of $(H/r)_{\text{p}}$ (Col. 7 of Table A1), and find $M_{\text{p}} > 1.0 M_{\text{th}}$ in every case. For this reason, we consider azimuthal wave modes down to the lowest possible m ($m = 1$ in the outer disk and $m = 2$ in the inner disk). We also consider $m \rightarrow \infty$, corresponding to the linear limit of Rafikov (2002) and the most tightly wound spirals (used in applications to observations by e.g., Muto et al. 2012; Casassus et al. 2021).

Observability. Using synthetic continuum observations, Speedie et al. (2022) found that the dust spirals driven by thermal mass planets at 50 au in a slowly cooling and moderately inclined ($i \lesssim 50^\circ$) disk 140 pc away are detectable in continuum observations with sensitivity between 10–25 $\mu\text{Jy beam}^{-1}$ and angular resolution ~ 30 –65 mas. Dong & Fung (2017) show that the amplitude of the spirals increases with planet mass for sub-thermal mass planets, and flattens out for super-thermal mass planets (their Fig. 1). In our sample, the inferred planet location is at a few tens to ~ 100 au, the mean beam size is $42 \pm 12 \times 54 \pm 17$ mas, the mean distance to the source is 144 ± 26 pc, the estimated continuum rms noises are all $\leq 22.6 \mu\text{Jy beam}^{-1}$ (except HD 97048), and only 2 disks are inclined by greater than 50° . We thus expect the current continuum observations to be sensitive to dust spirals driven by planets of thermal mass and above. Using the estimated $(H/r)_{\text{p}}$ (Col. 7, Table A1) and known M_* (Col. 3, Table A3) for each candidate in our sample, this $1.0 M_{\text{th}}$ lower limit translates to Jupiter masses ranging between 0.15–0.96 M_{Jup} (with 0.15 M_{Jup} corresponding to HD 143006, and 0.96 M_{Jup} to HD 97048).

Note that gravitational instability may also produce spiral arms in continuum emission detectable in ALMA residual maps (Hall et al. 2019), and they may interfere with planet-induced spirals (Rowther et al. 2022). We do not account for this complication in this work.

3. RESULTS & DISCUSSION

We find non-detections of dust spirals for 6 of the 10 candidate planets in our sample: DoAr 25, GW Lup, Sz 129, HD 163296 #2, P94, and HD 143006 (Fig. 1 & 2, §3.1). In 3 cases (Elias 27, IM Lup and WaOph 6), dust spirals are detected but their locations do not agree with that of the predicted planet (Fig. 4, §3.3). For the 10th candidate planet, HD 97048, the result is inconclusive (Fig. 3, §3.2).

3.1. Non-detections

Of the 6 non-detections of dust spirals, 3 correspond to velocity kinks that were classified as “tentative” detections (DoAr 25, GW Lup, Sz 129; Pin20). In these disks, we find no significant non-axisymmetric continuum substructure (Fig. 1).

Of the latter 3 non-detections (Fig. 2), 2 correspond to “firm” kink detections (HD 163296 #2, HD 143006; Pin20), and 1 to a kink detection with a radial and azimuthal significance of $(\sigma_r, \sigma_\phi) = (19.4, 7.5)$ (P94; Izq22). We find some small-scale non-axisymmetric continuum substructures in these disks, but none that agree with the predicted spiral wakes.

The above results persisted in additional imaging efforts we performed with the calibrated measurement sets for DoAr 25, GW Lup, Sz 129, HD 163296 and HD 143006, varying the Briggs parameter to maximize the observing sensitivity (see Appendix §C).

If the planets are there, why don't we see the dust spirals? One possibility is that the disks cool quickly, such that the dust temperature perturbation along the spiral wake is small, and does not enhance the spiral's intensity contrast (Speedie et al. 2022, see also Miranda & Rafikov 2020; Zhang & Zhu 2020). If that is the case, then we are mainly only probing the spiral *surface density* perturbation, which may be washed out at Band 6/7 wavelengths if the optical depth is sufficiently high. Follow-up at longer observing wavelengths may rule this possibility more or less likely. Additionally, in HD 163296 and HD 143006, the planet candidates are embedded in deep gaps and surrounded on either side by narrow rings. Only a small portion of the HD 163296 #2 and P94 spirals have the opportunity to be expressed upon the rings before they encounter the D48 gap or the outer edge of the continuum disk (Col. 4, Fig 2).

3.2. Inconclusive: HD 97048

We find strong and large-scale continuum residuals for the two assumed geometries (Cols. 7 & 8, Table A3) for HD 97048 (Fig. 3). Significant positive residuals in the inner disk align with the prediction for the inner spiral under both geometries, and the residuals show a portion of the outer spiral under the Ginski et al. (2016) geometry. It is unclear whether these matches support the planet hypothesis or are coincidental, because (a) the quality of the match depends on the geometry assumed, and (b) no matter what geometry we assume, there are significant residuals. Considering the possibility that

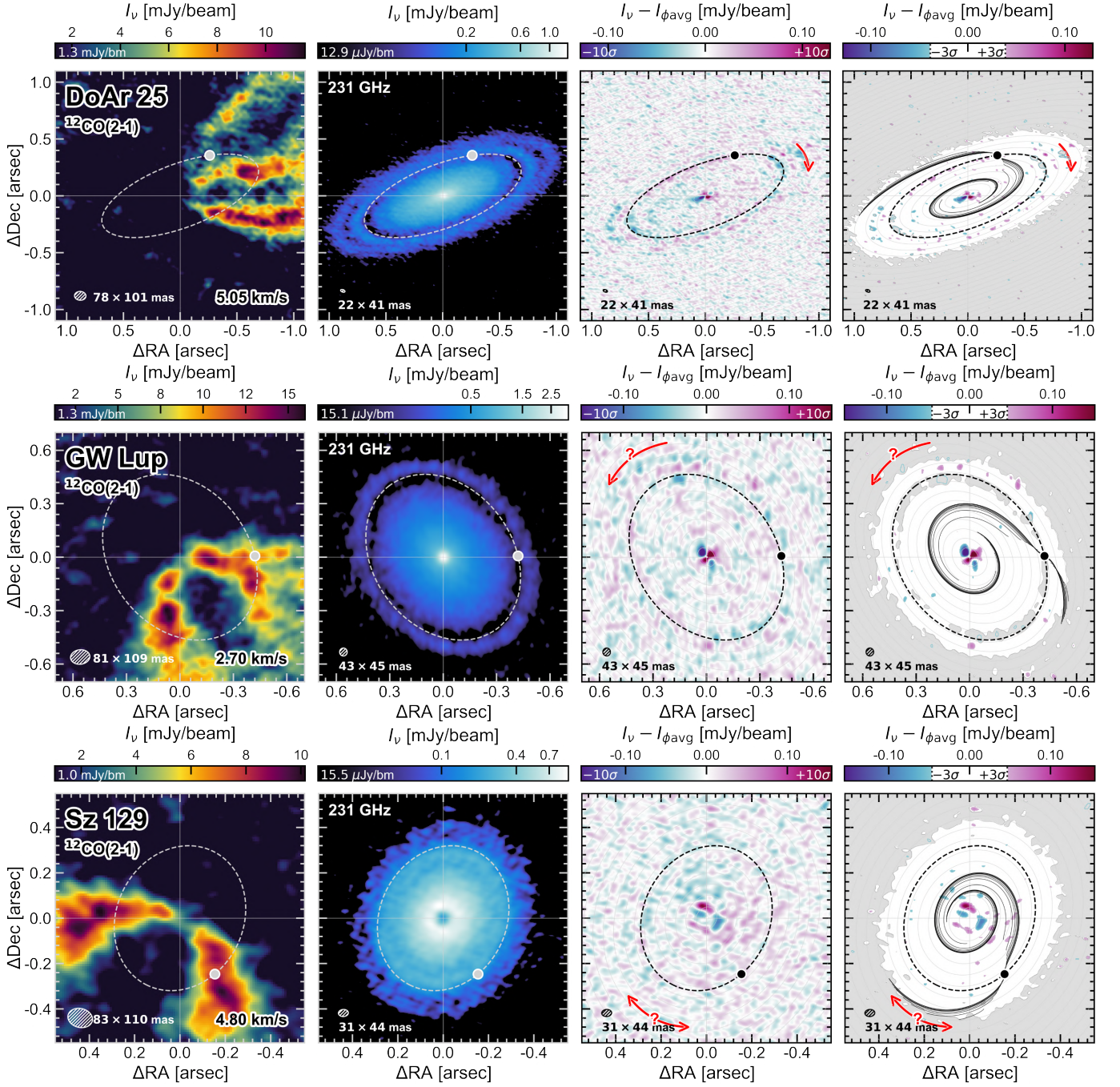


Figure 1. No clear detections of the predicted dust spirals: DoAr 25, GW Lup and Sz 129. In all columns, the grey or black point marks the reported planet location in the midplane, and the dashed grey or black line shows its circular orbit.

1st column: The CO channel map in which the velocity kink is most prominently detected. The estimated rms noise in the cube is written in the colorbar, and the colormap starts at that value.

2nd column: Continuum image showing where the planet lies relative to substructures in the dust distribution. The colormap starts at three times the rms noise (again written in the colorbar) and has a $\frac{1}{4}$ -power law stretch.

3rd column: Continuum residuals after subtracting the azimuthal average. Red arrows indicate the direction of rotation of the disk, and in all cases the arrow is located at the redshifted major axis. The colorbar spans $\pm 10\times$ the rms noise.

4th column: Comparison between detected residual substructures stronger than $3\times$ the continuum rms noise, and the theoretical prediction for the midplane spiral wake driven by the candidate planet (Bae & Zhu 2018a,b, our Eqn. 1). Light grey indicates where emission in the continuum image falls below this same threshold, helping to distinguish whether an absence of spiral-shaped residuals is due to the non-presence of spiral, or non-presence of emission (e.g. inside dust gaps or beyond the edge of the disk). Thin grey ellipses are projected concentric circles in radial steps of 1 beam major axis, helping to discern spirals from circular arcs under the angular resolution of the image.

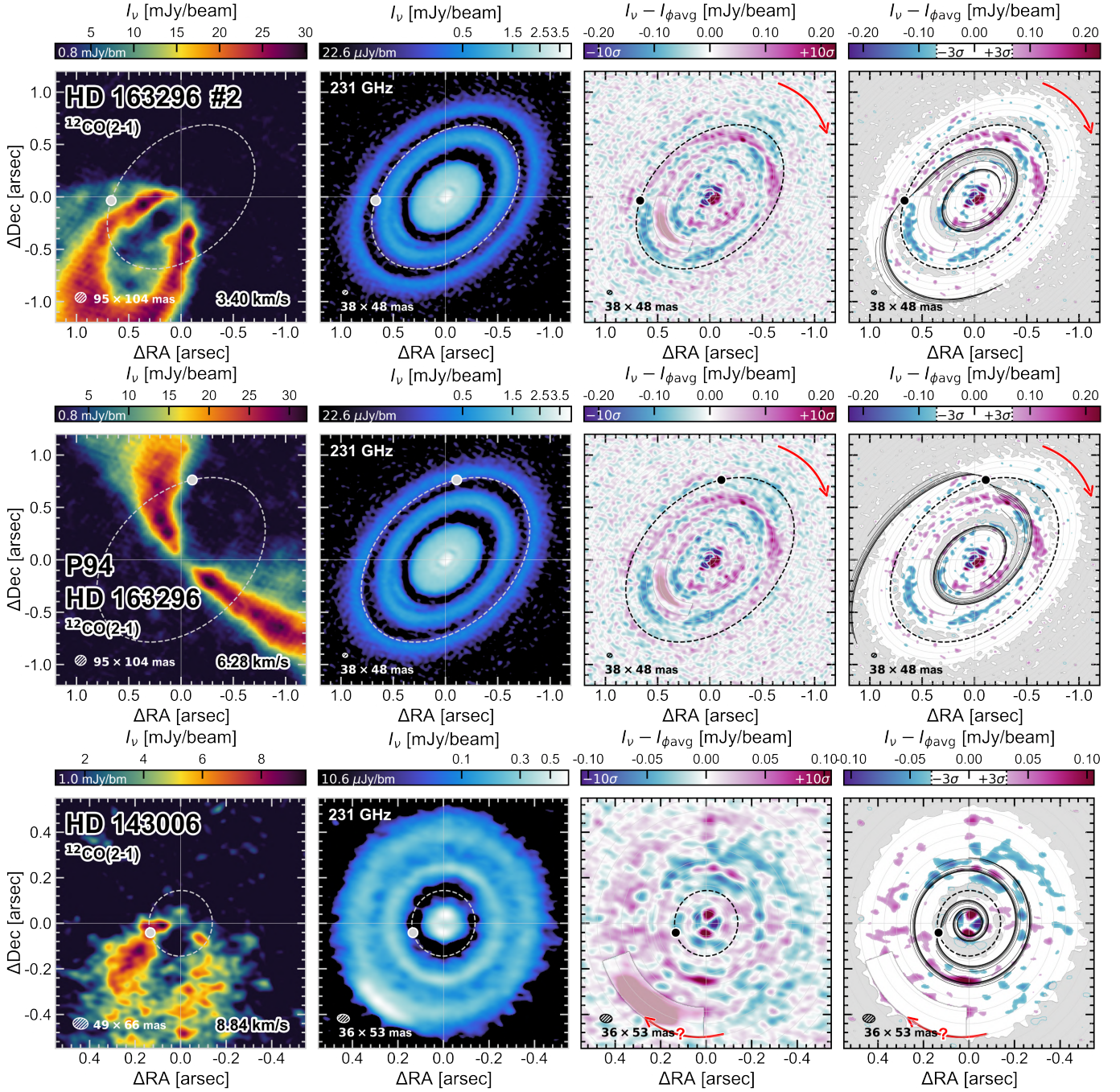


Figure 2. No clear detections of the predicted dust spirals (continued): HD 163296 #2, P94, and HD 143006. We mask the pronounced arc-like azimuthal asymmetries in these two disks to enhance the possibility of spiral detection (see Appendix Fig. B1).

Additional figures showing the continuum residuals after re-imaging the calibrated measurement sets with different Briggs parameters are available for HD 163296, HD 143006, DoAr 25, GW Lup and Sz 129 at DOI: [10.6084/m9.figshare.21330426](https://doi.org/10.6084/m9.figshare.21330426).

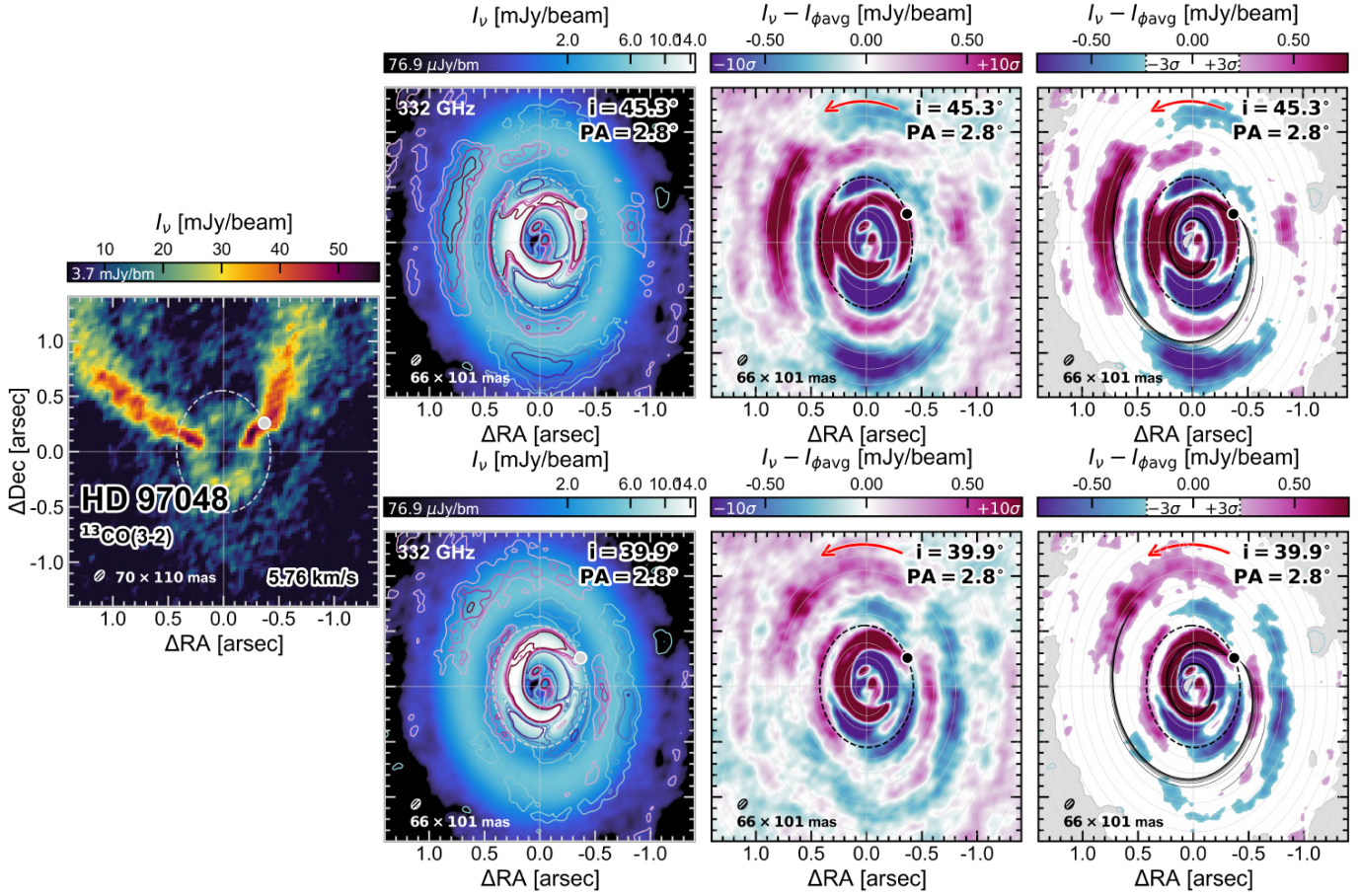


Figure 3. Inconclusive case: HD 97048. See §3.2 for details. Residual contours of $\pm 3, 5, 7, 10\times$ the continuum rms noise are overlaid in the 2nd column to help identify where residuals lie in relation to the gap and rings. *Top row:* Continuum residuals calculated assuming the disk geometry of Bohn et al. (2022). *Bottom row:* Continuum residuals calculated assuming the disk geometry of Ginski et al. (2016). Appendix Fig. D6 provides non-geometry-dependent residual maps for this disk.

these strong large-scale residuals indicate that an axisymmetric background model is not a good model, we attempt to find spiral residuals by a method that does not assume axisymmetry (Appendix Fig. D5), but come up empty-handed. We thus classify this case inconclusive.

3.3. Elias 27, IM Lup & WaOph 6

Of the 3 detections of dust spirals (Fig. 4), 2 correspond to velocity kinks that were classified as “firm” detections (Elias 27, IM Lup; Pin20), and 1 corresponds to a “tentative” kink detection (WaOph 6; Pin20). In all 3 cases, we see two spiral arms in the continuum residual maps, echoing Pérez et al. (2016) and Huang et al. (2018c).

Comparing the continuum residuals to the predicted spiral trajectories in Fig. 4, we find that the locations of the detected dust spirals in these 3 disks does not match with where we expect them to lie, given the predicted planet locations.

By comparing our estimation of $(H/r)_p$ and the reported estimates of the embedded planet masses (Cols. 7 & 8 of Table A1) to Figure 3 of Bae & Zhu (2018b), we see that the Elias 27, IM Lup and WaOph 6 planet candidates lie in a region of parameter space where we expect to see both a primary and secondary spiral in the inner disk. This may support the hypothesis that the observed two-armed spirals are planet-driven.

However, the two arms in these 3 disks are roughly symmetric, and simulations have shown that a planet-to-star mass ratio of $q \sim 0.01$ (or larger) is required to make symmetric inner primary and secondary spiral arms (Fig. 3, Fung & Dong 2015). This is a point of mild tension with the masses inferred from the velocity kink amplitude ($q \in [0.001, 0.005]$ in these 3 cases). Gravitational instability may be a better explanation for symmetric two-armed spirals (e.g., for Elias 27, see Meru et al. 2017; Tomida et al. 2017; Paneque-Carreño et al. 2021, and for such spirals in other disks, Dong et al. 2015).

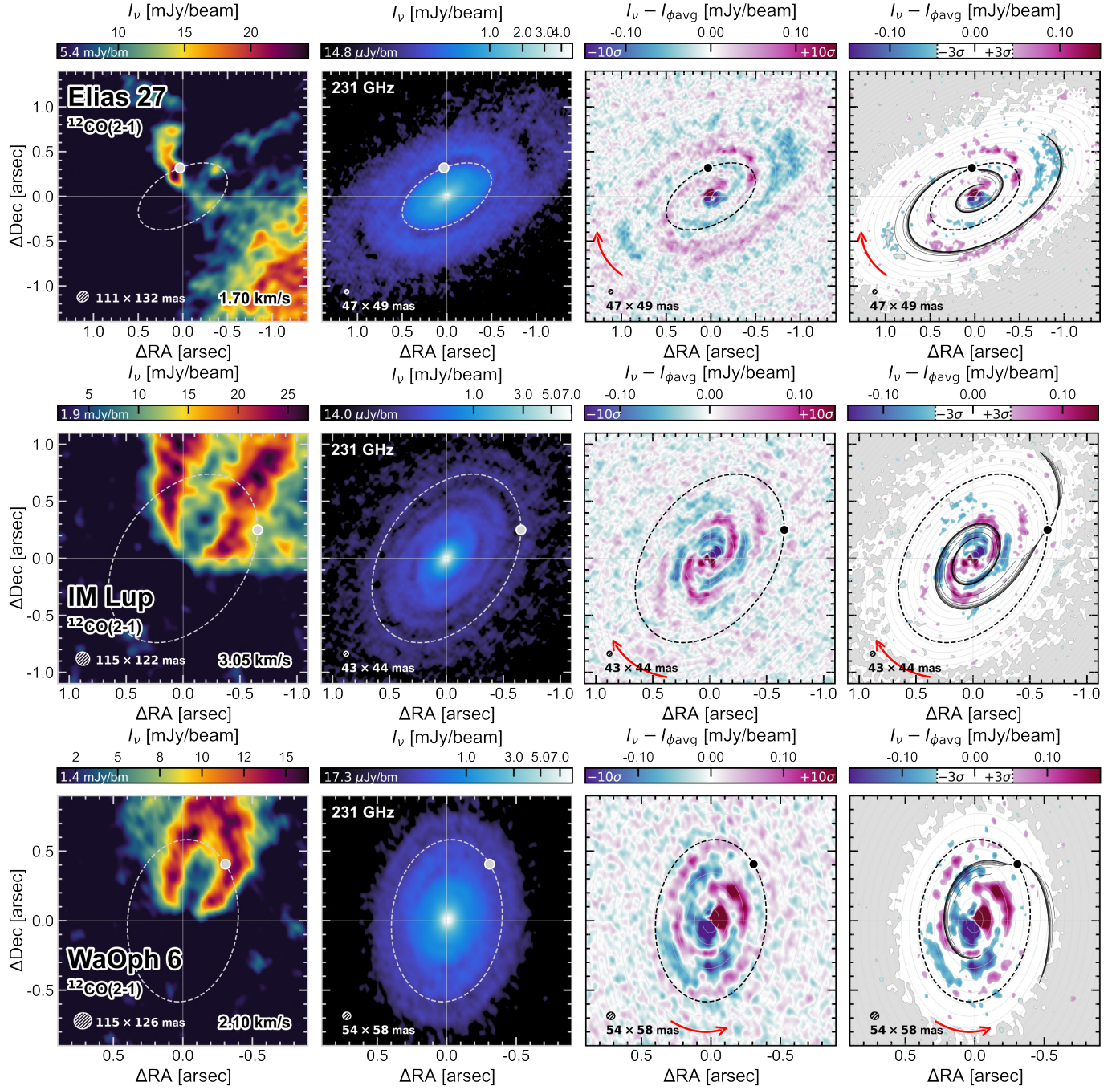


Figure 4. Detections of dust spirals offset from the predicted planet location: Elias 27, IM Lup and WaOph 6. The continuum spirals in these disks were first reported in Pérez et al. (2016) and Huang et al. (2018c).

As an alternative possibility that maintains the planetary-origin hypothesis, we contemplate the method used to determine the predicted planet locations (§2.1), which involves deprojecting the visually-identified kink center location from the estimated emission surface directly onto the midplane. Since the ^{12}CO emission surface is expected to be a few scale heights above the midplane (e.g., Pinte et al. 2018b; Law et al. 2021;

Paneque-Carreño et al. 2022), there may be room for error in translation. For example, Zhu et al. (2015) showed with 3D hydrodynamical simulations that spiral wakes are not perpendicular to the midplane, and instead curl towards the star at the disk surface. Vertical temperature gradients can introduce further complications, changing a spiral’s pitch angle and misaligning the surface wakes from the midplane wakes (Juhász &

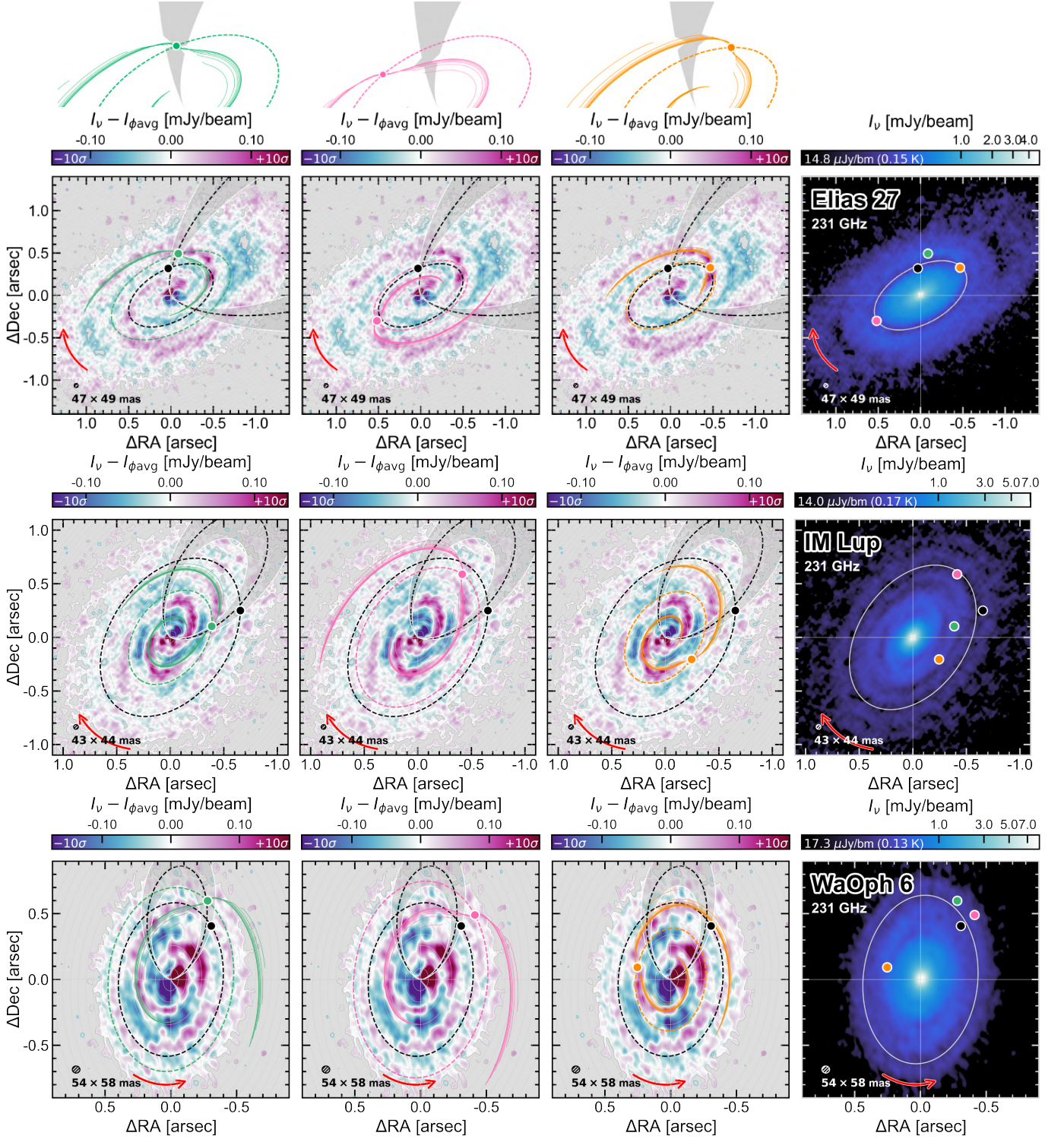


Figure 5. *Columns 1-3:* Alternative planet locations that achieve a better match to the observed continuum spiral residuals in Elias 27, IM Lup and WaOph 6, under three different restrictions (represented by the schematic at the top of each column; see §3.3 for details). The dashed black isovelocity contour is the velocity of the channel in which the kink is most prominently detected, and shaded grey regions demarcate $\pm 0.5 \times$ the channel width. In all columns, the black dot marks the deprojected kink location (shown in previous figures as representing the reported planet).

Column 4: Comparison between deprojected kink location and the alternative planet locations. The solid-line white ellipse is the DSHARP dust gap associated with the reported planet location (Col. 10 of Table 1).

Rosotti 2018; Rosotti et al. 2020). While Calcino et al. (2022) had success in matching ^{12}CO emission surface kinks around the full disk azimuth to the predicted spiral wake of HD 163296 #1 (P261), their simulations and analytic models assumed no vertical dependence in the velocity perturbations, and the location of this planet (which lies outside the continuum) has not been confirmed in midplane tracers. It’s therefore conceivable that the method for pinpointing the planet may need to encompass vertical effects. Motivated by the possibility of leveraging the location of the midplane continuum spirals to inform the development of such a method, we assume the spirals in Elias 27, IM Lup and WaOph 6 are planet-driven, and explore alternative planet locations.

3.3.1. Considering alternative planet locations

In the following, we present 3 alternative planet locations (shown left to right in Fig. 5) in each of Elias 27, IM Lup and WaOph 6, under a set of 3 informative and gradually loosening restrictions. In all cases, the restrictions are based on *midplane* information: the dust continuum residuals, the deprojected kink location, midplane isovelocity contours, and the 2D velocity kink theory of Bollati et al. (2021). We calculate the midplane isovelocity contours using the 2D Keplerian velocity field $v_0(R, \phi) = v_{\text{Kep}}(R) \sin(i) \cos(\phi) + v_{\text{LSR}}$, where i is the disk inclination, R and ϕ are the disk frame coordinates (ϕ measured from the redshifted disk major axis), and v_{LSR} is the systemic velocity. For v_{LSR} values see caption of Table A4.

In the 1st column of Fig. 5, we shift the planet location to get a better alignment with the detected dust spirals, under the restriction that the planet cannot lie outside the midplane area of the channel in which the velocity kink is most prominently detected. The motivation for this restriction is the idea that the velocity kink amplitude should be strongest close to the planet (e.g., Bollati et al. 2021; Calcino et al. 2022). We represent this area in grey, which spans a half channel width on either side of the velocity of the kink channel¹⁰ (Col. 6, Table 1) in order to incorporate the spatial “uncertainty” introduced by the spectral resolution of the CO data. We are able to achieve more satisfactory alignments, but find that the necessary shift in radial and azimuthal position places the planets outside their DSHARP dust gap (white solid ellipse in the 4th column).

At the top of Fig. 5, we show a midplane schematic of how we may expect the planet location to affect the emission morphology in a given channel (a logic-extension of the results from Bollati et al. 2021): if the

inner spiral wake shifts emission to lower velocity channels, and the outer wake shifts emission to higher velocity channels, then the channel centered on the planet may be left with an absence emission at the planet’s location. The kink (specifically, emission present in a channel that is spatially offset from the rest) may then instead be most prominent in a channel where it coincides with the inner or outer spiral wake.

Thus, in the 2nd and 3rd columns of Fig. 5, we again shift the planet location to get a better alignment with the detected dust spirals, but this time while maintaining that the reported kink is probing a portion of the planet’s inner spiral arm (2nd column) or outer spiral arm (3rd column), with the planet being as close to the deprojected kink location as possible. Under these two restrictions, we find some qualitative improvement in the match to the detected dust spiral, and in some cases (inner and outer wake scenario for Elias 27, inner wake scenario for IM Lup) we find that the resulting planet location lies inside the DSHARP dust gap. Important to note is that the *observed* midplane dust spiral residuals do not perfectly intersect with the deprojected kink location (and so the inner and outer wakes of our planet locations do not achieve perfect intersection either), suggesting a possible disjunction between midplane spirals and their expression on the disk surface.

We consider the 3 planet locations for each disk in Fig. 5 to be *possible* locations, in the sense that they plausibly satisfy the continuum spiral residuals. The main caveat is that we have not quantitatively assessed the agreement between the theoretical spiral trajectories and the continuum residuals, and obtained the planet locations by visual inspection / trial and error. We provide the locations in Table A4, and note that in some cases the planet in the midplane lies far from the deprojected velocity kink in ^{12}CO surface emission. As mentioned above, our determination of these planet locations was done using midplane-based information, without consideration for any surface velocity evidence associated with the new locations, and how the planets can reproduce the strength of the detected kink signals in a distant channel is unclear. It may not be the case that the channel in which the kink is intrinsically most prominent has been correctly identified in Elias 27 and WaOph 6, though, as the ^{12}CO channel maps of these 2 disks suffer cloud contamination. This applies to almost the entire redshifted (south) half of Elias 27, and a large portion of WaOph 6 from the disk minor axis toward the blueshifted (north) side (see note *a* in Table 1 for affected velocities).

Our results emphasize the need for more theoretical and simulation work to understand the expected morphology of a planet-driven velocity kink, how the planet’s spiral manifests at different heights in the disk, how the strength of the kink signal should vary with channel, and how we can use that information to successfully pinpoint the planet.

¹⁰ In the case of Elias 27, we infer from Table 2 and Fig. 1 of Pin20 that the kink is also detected in the two adjacent channels, though strong cloud contamination is present. In the case of Elias 27 and WaOph 6, it is unclear from their Table 2 whether the kink is detected in more than one channel. We thus opt to only consider the single channel.

4. SUMMARY

1. Despite the sufficiently high planet masses inferred from the reported velocity kink amplitudes, we are unsuccessful in detecting any dust spirals associated with 6 of the 10 velocity kink planet candidates reported to date whose orbits lie within the continuum disk, using current continuum observations (Figs. 1 & 2). We interpret this to mean that the full planet-finding potential of the velocity kink method may not be exemplified by this specific set of candidates. More kink detection efforts, including better quantification of the kink signal robustness and assessment for a planet-driven morphology, are needed.
2. Our search for dust spirals in the HD 97048 disk is inconclusive (Fig. 3). Observations with higher resolution and/or better sensitivity are needed to renew the search.
3. In the remaining 3 disks in our sample (Elias 27, IM Lup and WaOph 6), we re-detect clear and coherent dust spirals in the continuum residuals (Pérez et al. 2016; Huang et al. 2018c), but find that they do not align with the theoretical spiral trajectory originating at the candidate planet’s reported location (Fig. 4). If these spirals are planet-driven, then this spatial offset may indicate that the method used to pinpoint the planet location from the kink detection in these disks (§2.1) is incomplete; a more successful method may need to encompass how a midplane spiral can be “morphed” during its upward propagation to be expressed on the disk surface (§3.3). We provide alternative midplane planet locations that are plausible from the dust spiral’s perspective for these 3 planet candidates in Fig. 5 and Table A4, which in some cases are far from the reported velocity kink (§3.3.1).

We thank the anonymous referee for their thoughtful and constructive questions and suggestions. J.S. thanks Richard Booth, Cathie Clarke, Giovanni Rosotti, Richard Alexander, Richard Nelson, Brodie Norfolk, Rebecca Nealon, Sahl Rowther, Giulia Ballabio, Simon Casassus, Sebastián Pérez and Philipp Weber for insightful discussions that helped shape this work, and we thank Daniel Price for comments on the manuscript. J.S. also thanks the curator of the Catalog of Circumstellar Disks (www.circumstellardisks.org). R.D. and J.S. are supported by the Natural Sciences and Engineering Research Council of Canada (NSERC) and the Alfred P. Sloan Foundation.

We are grateful to Christophe Pinte and DSHARP Collaboration for making their data publicly available. This paper makes use of the following ALMA data: ADS/JAO.ALMA #2016.1.00484.L, ADS/JAO.ALMA #2016.1.00825.S. ALMA is a partnership of ESO (representing its member states), NSF (USA) and NINS (Japan), together with NRC (Canada), MOST and ASIAA (Taiwan), and KASI (Republic of Korea), in cooperation with the Republic of Chile. The Joint ALMA Observatory is operated by ESO, AUI/NRAO and NAOJ. The National Radio Astronomy Observatory is a facility of the National Science Foundation operated under cooperative agreement by Associated Universities, Inc. This work has made use of data from the European Space Agency (ESA) mission *Gaia* (<https://www.cosmos.esa.int/gaia>), processed by the *Gaia* Data Processing and Analysis Consortium (DPAC, <https://www.cosmos.esa.int/web/gaia/dpac/consortium>). Funding for the DPAC has been provided by national institutions, in particular the institutions participating in the *Gaia* Multilateral Agreement.

Facility: ALMA.

Software: `astropy` (Astropy Collaboration et al. 2013, 2018), `cmasher` (van der Velden 2020), `disksurf` (Teague et al. 2021a), `gofish` (Teague 2019b), `matplotlib` (Hunter 2007), `numpy` (Harris et al. 2020), `pandas` (The pandas development team 2020), `scipy` (Virtanen et al. 2020).

APPENDIX

A. TABLES

Tables A1, A2, A3 and A4.

B. TREATMENT OF CONFINED AZIMUTHAL ASYMMETRIES

The strong emission from the confined arc-like features in HD 163296 and HD 143006 will, of course, raise the azimuthal average emission within the radial region that they occupy, therefore making it more difficult to

detect any dust spirals above the (overly-positive) average background in that radial region. This is particularly relevant for our search in HD 163296, as the inner spiral wake of both the HD 163296 #2 and P94 planets would be expressed upon the B67 ring, which is contaminated by the arc-like feature. It is less important for our search in HD 143006, because the candidate planet’s spiral wake is tightly wound and unlikely to “reach” the radial region occupied by the crescent. In HD 163296, we omit from the calculation of the azimuthal average

Table A1. Inferred midplane locations of planets detected by a velocity kink inside the continuum.

Disk	Ref.	Planet Sky Coordinates		Planet Disk Frame Coordinates		$(H/r)_p$	M_p
		r_p	PA_p	R_p	ϕ_p		
		($''$)	(deg)	(au)	(deg)		(M_{th})
(1)	(2)	(3)	(4)	(5)	(6)	(7)	(8)
Elias 27	Pin20	$0.32 \pm \dots$	$6 \pm \dots$	$60 \pm \dots$	$-103 \pm \dots$	0.087	$3.0 - 8.9$
HD 143006	Pin20	$0.14 \pm \dots$	$107 \pm \dots$	$24 \pm \dots$	$-61 \pm \dots$	0.043	$6.5 - 19.6$
HD 163296 (P94)	Izq22	0.77 ± 0.05	-8 ± 3	94 ± 6	50 ± 3	0.069	$1.4 - 4.3$
HD 163296 (#2)	Pin20	$0.67 \pm \dots$	$93 \pm \dots$	$82 \pm \dots$	$129 \pm \dots$	0.066	$1.6 - 4.8$
IM Lup	Pin20	$0.70 \pm \dots$	$-69 \pm \dots$	$127 \pm \dots$	$136 \pm \dots$	0.089	$1.5 - 4.6$
DoAr 25	Pin20	$0.44 \pm \dots$	$-36 \pm \dots$	$101 \pm \dots$	$60 \pm \dots$	0.071	$2.8 - 8.3$
GW Lup	Pin20	$0.42 \pm \dots$	$-89 \pm \dots$	$78 \pm \dots$	$-119 \pm \dots$	0.084	$3.5 - 10.4$
Sz 129	Pin20	$0.29 \pm \dots$	$-148 \pm \dots$	$53 \pm \dots$	$63 \pm \dots$	0.059	$5.6 - 16.8$
WaOph 6	Pin20	$0.51 \pm \dots$	$-37 \pm \dots$	$72 \pm \dots$	$138 \pm \dots$	0.089	$2.0 - 6.0$
HD 97048	Pin19	0.45 ± 0.10	-55 ± 10	109 ± 24	-66 ± 10	0.073	$2.1 - 3.1$

NOTE—Column descriptions: (1) Name of disk. Name of kink or planet candidate in brackets, if applicable. (2) Reporting paper, as in Table 1. (3-4) Coordinates of the planet as seen on the sky: Radial separation from the star (r_p), and position angle measured east of north (PA_p). The ‘...’ indicates where authors gave no indication of uncertainty. Note that Pin20 (their Table 1) provides PA_p measured *west* of north. (5-6) Coordinates of the planet in the disk frame: Radius in the deprojected midplane (R_p), and polar angle measured anti-clockwise from the disk’s redshifted major axis (ϕ_p). Disk frame coordinates were calculated by this work, with the exception of row 3 (P94, Izq22), in which case we calculated the sky frame coordinates. Values of d used for arcsec \leftrightarrow au are in Table A3. (6) Aspect ratio (H/r) evaluated at R_p , calculated by this work using Eqn. 3 and L_* in Table A3. (7) Mass estimate of the planet in units of thermal mass M_{th} , calculated by this work using Column 6, M_* in Table A3, and the M_p range in units of M_{Jup} from the reporting paper (Column 11 of Table 1).

Table A2. Summary of observations used in this work.

Disk	Origin	CO		Continuum	
		rms noise	θ_{beam}	rms noise	θ_{beam}
		(mJy/bm)	(mas)	(μ Jy/bm)	(mas)
(1)	(2)	(3)	(4)	(5)	(6)
Elias 27	DDR	1.6	111×132	14.8	47×49
HD 143006	DDR	1.0	49×66	10.7	36×53
HD 163296	DDR	0.8	95×104	22.6	38×48
IM Lup	DDR	1.9	115×122	14.0	43×44
DoAr 25	DDR	1.3	78×101	12.9	22×41
GW Lup	DDR	1.3	81×109	15.1	43×45
Sz 129	DDR	1.0	83×110	15.5	31×44
WaOph 6	DDR	1.4	115×126	17.3	54×58
HD 97048	FS	3.7	70×110	76.9	66×101

NOTE—Column descriptions: (1) Name of source. (2) DDR: [DSHARP Data Repository](#) (Program ID: 2016.1.00484.L), FS: [Figshare](#) (Program ID: 2016.1.00825.S). (3) Measured rms noise in the cube. (4) Synthesized beam FWHM of the cube. (5) Measured rms noise in the image. The values in Column 3 & 5 are almost identical to those of [Andrews et al. \(2018\)](#) (Table 4 & 5) and [Pinte et al. \(2019\)](#). (6) Synthesized beam FWHM of the continuum image.

the emission lying within $135^\circ \leq \phi \leq 220^\circ$ between $R = 0.49''$ and $R = 0.63''$, where R and ϕ are disk frame coordinates (ϕ measured anti-clockwise from the

redshifted disk major axis). In HD 143006, we omit the emission lying within $-58^\circ \leq \phi \leq 12^\circ$ between $R = 0.37''$ and $R = 0.5''$.

Fig. B1 shows the continuum residual maps in HD 163296 and HD 143006 with and without including the confined arc-like features in the azimuthal average. In HD 163296, excluding the arc-like feature modifies the residuals in a way that is more relevant for the HD 163296 #2 planet candidate than for P94 (hence why it is plotted in Fig. B1 instead of P94) – some disconnected positive residuals are introduced in the northeast portion of the radial region (where HD 163296 #2’s inner spiral would lie), though they do not appear to be a segment of a spiral. In HD 143006, excluding the arc-like feature removes the strongly negative residuals in the west half of the disk, but doesn’t affect the residuals near the planet candidate.

C. RE-IMAGING THE CONTINUUM VISIBILITIES TO ACHIEVE HIGHER SENSITIVITY

[Speedie et al. \(2022\)](#) argued that a beam size ~ 2 times larger than the width of the spiral can yield a higher signal-to-noise detection in a residual map than a higher angular resolution image. Motivated by this, we re-imaged the publicly available DSHARP calibrated measurement sets of the 5 disks whose fiducial images yielded non-detections (DoAr 25, GW Lup, Sz 129, HD 163296 and HD 143006), varying the Briggs parameter

Table A3. Stellar properties and disk geometries.

Disk	d	M_*	L_*	Disk geometry					Rotation
				Δx	Δy	i	PA	Method	
	(pc)	(M_\odot)	(L_\odot)	(mas)	(mas)	(deg)	(deg)		
(1)	(2)	(3)	(4)	(5)	(6)	(7)	(8)	(9)	(10)
Elias 27	110.1 ± 10.3	$0.49^{+0.20}_{-0.11}$	$0.91^{+0.64}_{-0.37}$	-5 ± 5	-8 ± 3	56.2 ± 0.8	118.8 ± 0.7	E	CW
HD 143006	167.3 ± 0.5	$1.78^{+0.22}_{-0.30}$	$3.8^{+1.6}_{-1.1}$	$-6 \pm \sim 2$	$23 \pm \sim 2$	$16 \pm \sim 2$	$167 \pm \sim 2$	FRANK	CW?
HD 163296	101.0 ± 0.4	$2.04^{+0.25}_{-0.13}$	$17.0^{+1.7}_{-8.5}$	$-3.5 \pm \sim 2$	$4 \pm \sim 2$	$47 \pm \sim 2$	$313 \pm \sim 2$	FRANK	CW
IM Lup	155.8 ± 0.5	$0.89^{+0.21}_{-0.23}$	$2.6^{+1.5}_{-0.95}$	-1.5 ± 2	1 ± 2	47.5 ± 0.3	144.5 ± 0.5	E	CW
DoAr 25	138.2 ± 0.8	$0.95^{+0.10}_{-0.33}$	$1.0^{+0.56}_{-0.35}$	38 ± 2	-494 ± 2	67.4 ± 0.2	290.6 ± 0.2	E	CW
GW Lup	155.2 ± 0.4	$0.46^{+0.12}_{-0.15}$	$0.33^{+0.19}_{-0.12}$	$0.5 \pm \sim 2$	$-0.5 \pm \sim 2$	$39 \pm \sim 2$	$37 \pm \sim 2$	FRANK	ACW?
Sz 129	160.1 ± 0.4	$0.83^{+0.06}_{-0.24}$	$0.44^{+0.26}_{-0.16}$	$5 \pm \sim 2$	$6 \pm \sim 2$	$32 \pm \sim 2$	$153 \pm \sim 2$	FRANK	?
WaOph 6	122.5 ± 0.4	$0.68^{+0.32}_{-0.13}$	$2.9^{+1.7}_{-1.0}$	-244 ± 3	-361 ± 3	47.3 ± 0.7	174.2 ± 0.8	E	ACW
HD 97048	184.4 ± 0.8	2.36 ± 0.19	36.6 ± 20.03	0	0	45.3 ± 2.55	2.84 ± 2.55	Velocity Field	ACW
				0	0	39.9 ± 1.8	2.8 ± 1.6	Scattered Light	

NOTE—Column descriptions: (1) Name of source. (2) Distance to the source, from *Gaia* DR3 (Gaia Collaboration et al. 2016, 2022) as $d = 1/\varpi$. (3) Stellar mass. (4) Stellar luminosity. Values for L_* , and M_* are from Andrews et al. (2018) except HD 97048, in which case L_* and M_* are from Bohn et al. (2022). (5) R.A. offset of disk center from phase center (in the datasets we use; see Table A2). (6) Decl. offset of disk center from phase center. (7) Disk inclination. (8) Disk position angle, measured anti-clockwise (i.e., east of north) to the red-shifted major axis. (9) Method used to estimate disk P.A., inclination, and offset from phase center in the work from which we source the values: “E” indicates that the values were derived by fitting ellipses to continuum annular substructures (Table 2, Huang et al. 2018b); “FRANK” indicates the frank residual appearance method of Andrews et al. (2021) (their Table 2); “Velocity Field” indicates the results of fitting a Keplerian disk model to the velocity field from CO line data cubes (Table C.1, Bohn et al. 2022) with eddy (Teague 2019a); and “Scattered Light” indicates the results of fitting ellipses to gaps and rings observed in near-IR scattered light by SPHERE (Table 1, Ginski et al. 2016). (10) Direction in which the disk rotates. “CW” means clockwise (west of north) and “ACW” means anti-clockwise. Rotation direction for Elias 27 and WaOph 6 were taken from Huang et al. (2018c); the remaining disk rotations were determined by this work based on scattered light observations in the following works: Elias 27 (Huang et al. 2018c), HD 143006 (Benisty et al. 2018; Pérez et al. 2018), HD 163296 (Monnier et al. 2017; Muro-Arena et al. 2018), IM Lup (Avenhaus et al. 2018; Huang et al. 2018c), DoAr 25 (Andrews et al. 2008; Garufi et al. 2020), GW Lup (Garufi et al. 2022), Sz 129 (none to our knowledge), WaOph 6 (Huang et al. 2018c), HD 97048 (Ginski et al. 2016). “?” indicates cases where the near/far side is uncertain or unknown in scattered light images in the literature to date (note the low inclination of those 3 disks).

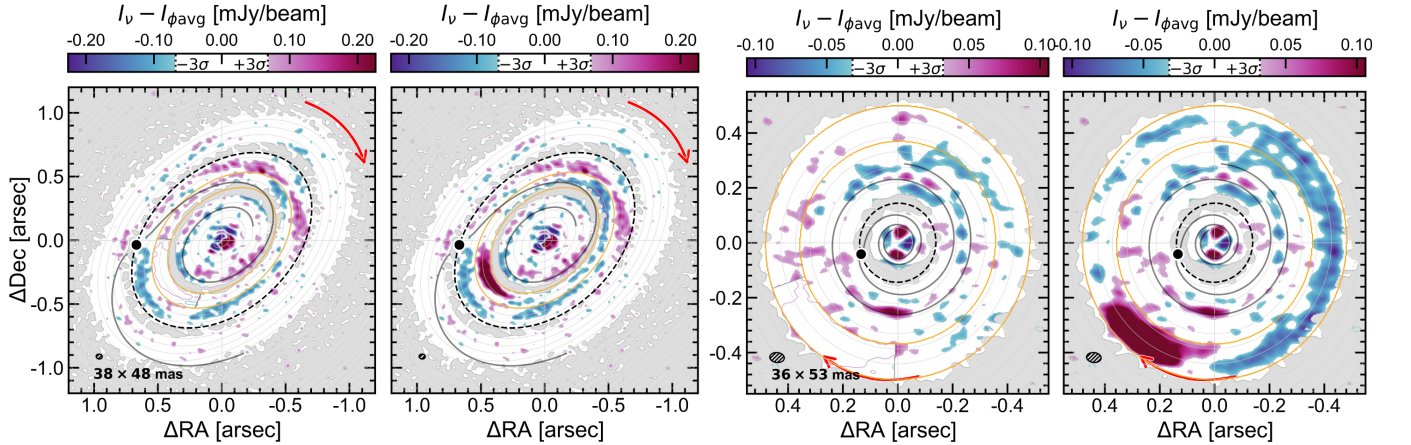


Figure B1. Treatment of crescents in HD 163296 and HD 143006: Detected residual substructures stronger than $3\times$ the continuum rms noise in HD 163296 (left two panels) and HD 143006 (right two panels) when either including or excluding the confined arc-like azimuthal asymmetries. The two orange ellipses guide the eye to the radial region affected (i.e., the residual maps are identical outside of this region). A 3σ contour of the arc-like feature is shown under the mask to demonstrate how the mask covers the feature.

Table A4. Coordinates of the alternative planet locations presented in Fig. 5.

Disk	Col.	Sky Coordinates		Disk Frame Coords.		v_p
		r_p	PA_p	R_p	ϕ_p	
(1)	(2)	(3)	(4)	(5)	(6)	(7)
Elias 27	1	0.50	-10	85	-114	1.65
	2	0.60	120	66	2	4.48
	3	0.57	-55	64	191	0.31
IM Lup	1	0.40	-75	76	129	2.99
	2	0.72	-35	112	-179	2.51
	3	0.32	-130	74	87	4.57
WaOph 6	1	0.66	-25	86	153	2.13
	2	0.64	-40	92	135	2.53
	3	0.27	70	48	-100	3.40

NOTE—Column descriptions: (1) Name of disk. (2) Column of Fig. 5 showing the planet whose coordinates are given, numbered 1 to 3, left to right. (3-4) Coordinates of the planet as seen on the sky: Radial separation from the star (r_p), and position angle measured east of north (PA_p). (5-6) Coordinates of the planet in the disk frame: Radius in the deprojected midplane (R_p), and polar angle measured anti-clockwise from the disk’s redshifted major axis (ϕ_p). Values of d used for arcsec \leftrightarrow au are in Table A3. (7) Velocity coordinate of the planet, relative to Earth. Systemic velocities used to find these values were estimated from the morphology of emission in the channel maps (thus having uncertainty v_{sys} , Col. 5 of Table 1), and are: $v_{\text{LSR}} = 2.40$ km/s for Elias 27, $v_{\text{LSR}} = 4.45$ km/s for IM Lup and $v_{\text{LSR}} = 3.85$ km/s for WaOph 6.

to explore the full available range of angular resolutions and achievable sensitivities. We show an example of the results in Fig. C2. The full set is available at DOI: [10.6084/m9.figshare.21330426](https://doi.org/10.6084/m9.figshare.21330426).

D. METHODS FOR DETECTING DUST SPIRALS

D.1. Comparison with *frank*

All 8 of the DSHARP disks in our sample were analyzed in uv -space with *frank* by Jennings et al. (2022a), and 4 of them also by Andrews et al. (2021). Those works did not report detections of dust spirals in the *frank* residual maps of DoAr 25, GW Lup, Sz 129 and HD 163296, a result echoed by this letter. Side-by-side comparisons between the imaged *frank* residuals and our image-plane residuals shows the techniques give nearly identical results.

Andrews et al. (2021) report a “low-level” tentative large-scale Archimedean spiral in HD 143006 (their Fig. 4). In our Fig. D3, we re-present the continuum residuals we obtained for HD 143006 (the exact same map as appears in the main text in the bottom right panel of Fig. 2), on the same colour scale as Andrews et al. (2021), to more clearly demonstrate the extent to which our azimuthal average technique recovers this tentative spiral. The basic result is similar, and our method recovers the spotty residual features along the Andrews

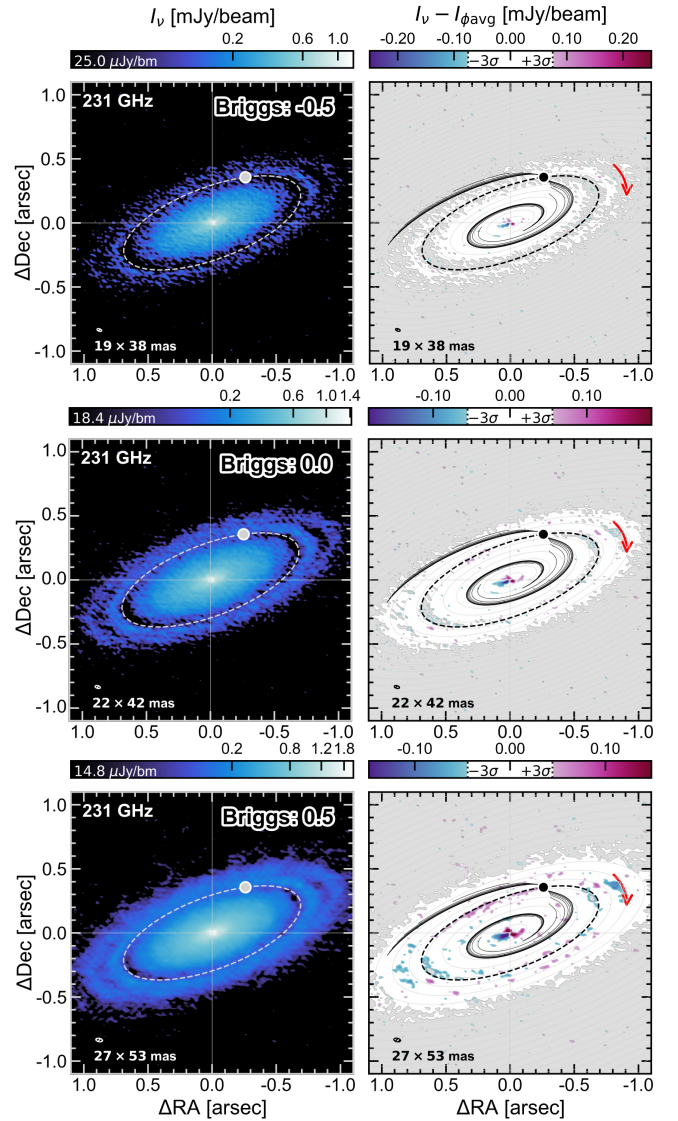


Figure C2. Subset of our re-imaging efforts with higher Briggs parameters to increase the beam width and sensitivity, showing the disk DoAr 25 as an example. The full set of images for DoAr 25, Sz 129, GW Lup, HD 163296 and HD 143006 for Briggs parameters $\in [-1, -0.5, -0.3, 0, 0.3, 0.5, 1, 2]$ is available at: DOI: [10.6084/m9.figshare.21330426](https://doi.org/10.6084/m9.figshare.21330426).

et al. (2021) spiral. In this case, some differences in the residuals can be attributed to the differing treatments of the confined azimuthal asymmetries. We note that the direction of this spiral (assuming it is trailing) implies counter-clockwise rotation for the HD 143006 disk, opposite to the clockwise rotation suggested by Pérez et al. (2018).

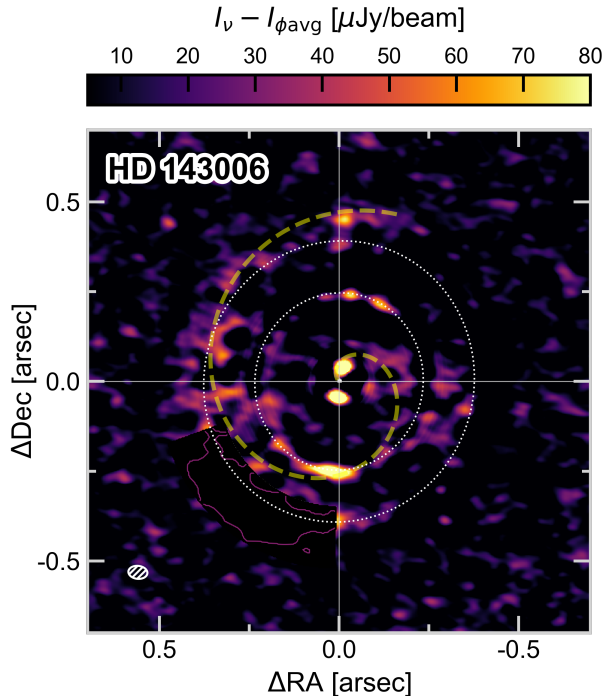


Figure D3. A re-presentation of our azimuthal average continuum residual map for HD 143006, for comparison to Fig. 4 of Andrews et al. (2021). The dashed yellow curve is their (visually tuned, not fit) Archimedean spiral overlay, described in disk-frame coordinates by $R_{\text{spiral}} = 0.170 + 0.067\phi$ [arcsec]. The two dotted white ellipses mark the DSHARP-identified rings, B41 and B65.

D.2. Additional Searches with the Unsharp Masking Method

One of the most significant challenges to using the azimuthal average as a background model is that it makes assumptions on the disk geometry – namely, that the dust disk is inherently axisymmetric and planar, and that one has accurate knowledge of the disk inclination and position angle. Artificial residuals can be introduced if one uses the incorrect disk geometry. Creating residual maps with `frank` (Jennings et al. 2020) involves the same challenges (e.g., Appendix A of both Jennings et al. 2022b; Andrews et al. 2021).

In this section we explore an alternative technique that makes no assumptions on the disk geometry, and apply it to the disks that exhibited small- or large-scale

azimuthal average residuals: HD 163296, HD 143006, and HD 97048. The technique has been referred to as “unsharp masking” (e.g., Pérez et al. 2016; Meru et al. 2017), and involves convolving the observation with a normalized 2D Gaussian of HRFM $\sigma_{x,y}$ and subtracting the result from the original image. It is mathematically equivalent to the “high-pass filtering” technique (e.g., Rosotti et al. 2020; Norfolk et al. 2022) which involves suppressing large-scale spatial (angular) frequencies by convolution with a 1D Gaussian of HRFM σ_ν in the Fourier domain. We confirmed both give identical residual maps with the appropriately-scaled Gaussian kernels ($\sigma_\nu = 2\pi/\sigma_{x,y}$), but only show the former here so as to consistently work in the image plane.

Fig. D4 compares the efficacy of the residual-making method we use in the main body of the paper to that of the unsharp masking method, using a synthetic continuum observation model¹¹ from Speedie et al. (2022). To produce the unsharp masking residual map, we convolve the model image (I_ν , 1st panel) with a 2D Gaussian of HRFM $\sigma_{x,y} = 30$ mas (I_{conv} , 4th panel) using `scipy.ndimage.gaussian_filter`. The residuals resulting from different kernel sizes will vary in morphology, as different kernels sequentially highlight different spatial scales of the image structures, and in practise we strongly encourage the observer to view the results for a range of $\sigma_{x,y}$. Here, we show the results for a select $\sigma_{x,y}$, chosen such that I_{conv} is smoothed of blobs but still contains the radial structure present in I_ν . This figure shows that the unsharp masking method can be effective, though it is prone to accentuating gaps and rings.

Nonetheless, for its main benefit of not requiring assumptions on the disk geometry, we apply it to the continuum observations of HD 163296, HD 143006 and HD 97048 in Figs. D5 & D6. In the resulting residual maps for HD 163296 and HD 143006 (5th column of Fig. D5), we detect only ring and gap structures and no spirals, consistent with the azimuthal average method in the main text. In HD 97048 (Fig. D6), we find that a single 2D Gaussian kernel does not highlight substructure in both the inner and outer ring simultaneously, and so we show the results for both a $\sigma_{x,y} = 60$ mas kernel and a $\sigma_{x,y} = 30$ mas kernel. The residual map produced with the larger kernel (2nd panel, Fig. D6) shows no spiral structure in the outer ring. The residual map produced with the smaller kernel (3rd panel, Fig. D6) reveals a double-ring structure over $\sim 270^\circ$ of the inner ring, but no residuals that consistently follow the predicted trajectory for the planet’s inner spiral arm.

REFERENCES

¹¹ Downloadable from Figshare: [10.6084/m9.figshare.19148912](https://figshare.com/10.6084/m9.figshare.19148912). This model contains a $1.0 M_{\text{th}}$ mass planet at 50 au in an adiabatic, slowly cooling ($\beta = 10$), marginally optically thin ($\tau_0 = 0.3$) disk at a distance of 140 pc, observed with the C5+C8 ALMA configuration pair for an on-source time of 3.56 hours.

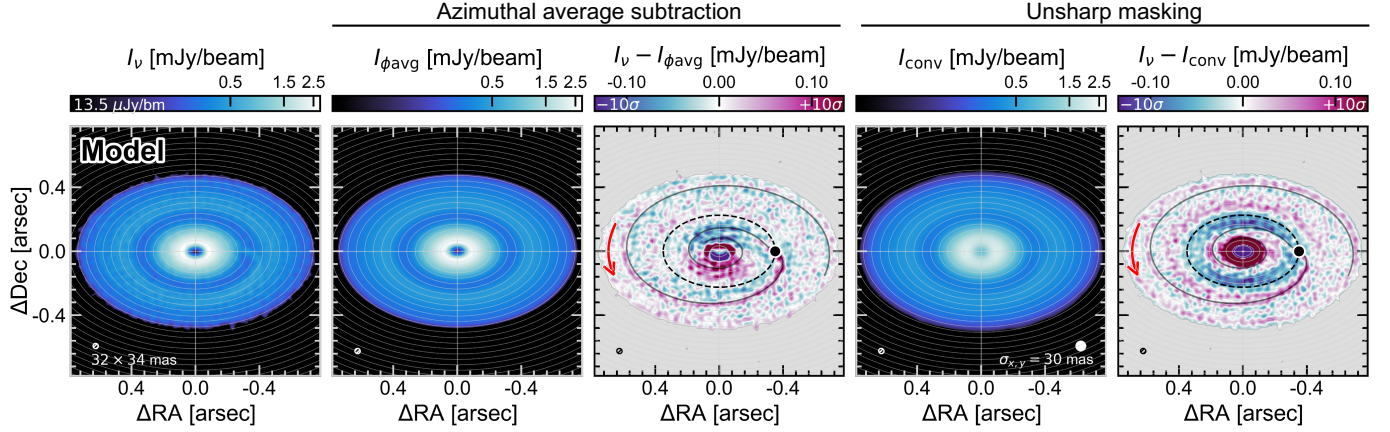


Figure D4. Comparing methods for detecting planet-driven dust spirals: Azimuthal average subtraction vs. unsharp masking. *1st panel:* Synthetic continuum observation, I_ν . *2nd panel:* Background disk model $I_{\phi\text{avg}}$ obtained by azimuthally averaging I_ν , using knowledge of the disk inclination, position angle and phase offset. *3rd panel:* Residual map as the difference between I_ν and $I_{\phi\text{avg}}$. *4th panel:* Background disk model I_{conv} obtained by convolving I_ν with a 2D Gaussian kernel of HWHM $\sigma_{x,y}$, making no assumptions on the disk geometry. Filled white circle represents the Gaussian kernel. *5th panel:* Residual map as the difference between I_ν and I_{conv} .

In the residual maps, we overlay the theoretical prediction for the midplane spiral wake driven by the model planet (Bae & Zhu 2018a,b, our Eqn. 1), whose mass is $M_p = 1.0 M_{\text{th}}$. Only the dominant azimuthal mode ($m_{\text{dom}} = (\frac{1}{2})(H/r)_p^{-1}$) is shown, and the planet's outer spiral wake becomes more open than the predicted trajectory with distance from the planet.

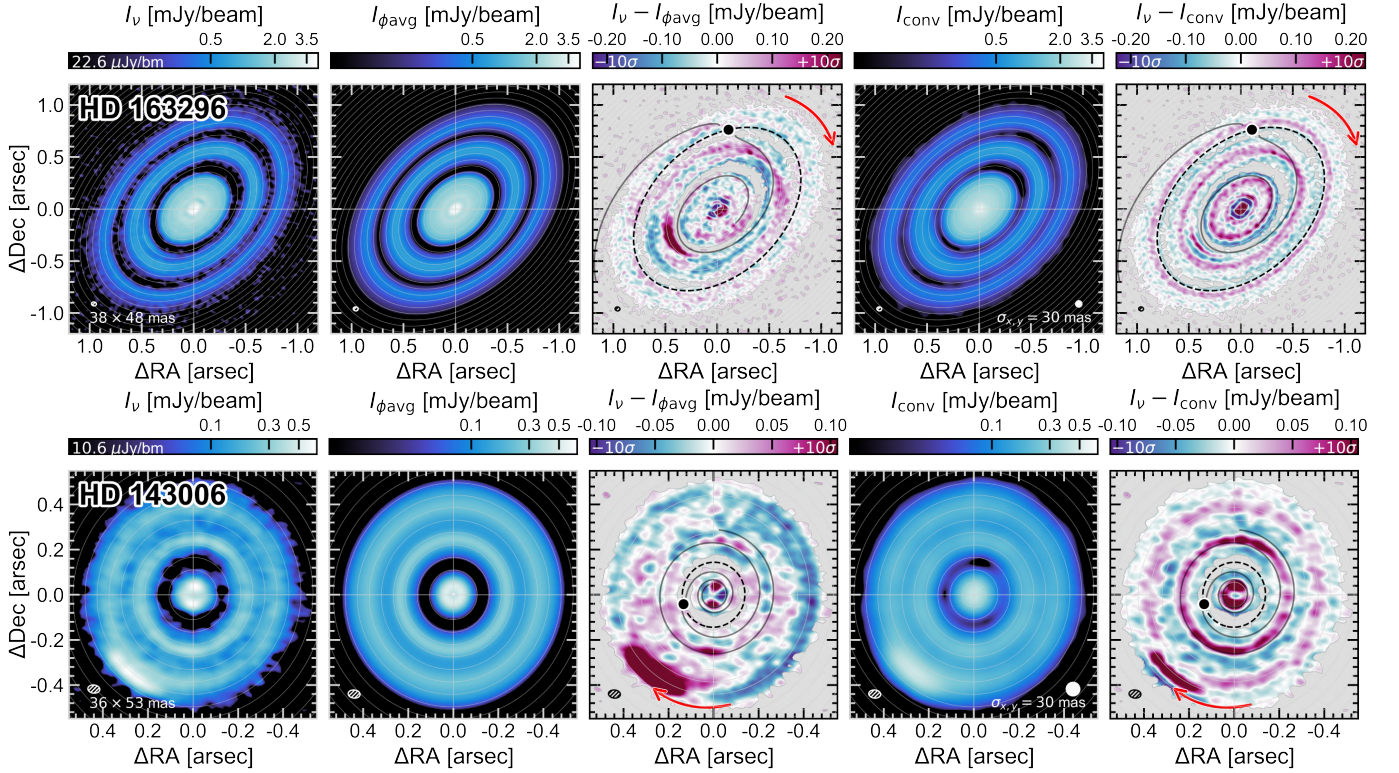


Figure D5. Additional searches for the predicted dust spirals: HD 163296 and HD 143006. Panel layout similar to Fig. D4.

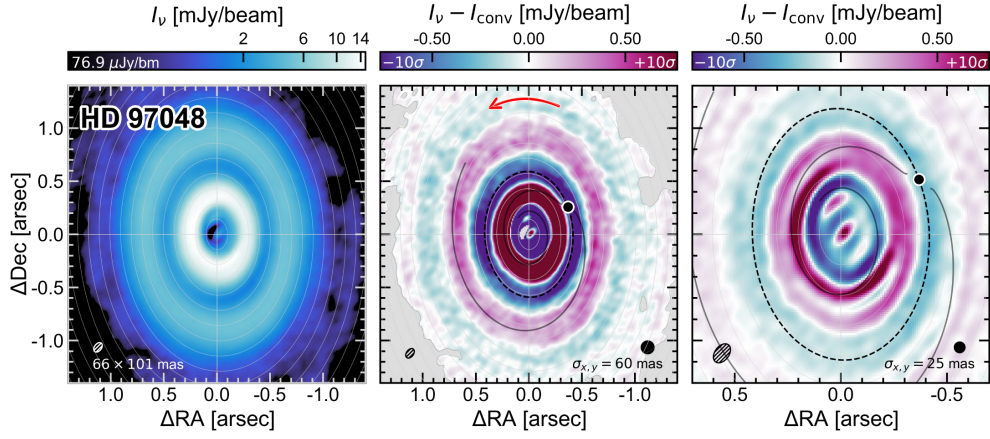


Figure D6. Additional searches for the predicted dust spirals: HD 97048. Unsharp masking residuals produced with two 2D Gaussian kernels of different sizes to highlight substructure in the outer ring (*2nd panel*) and inner ring (*3rd panel*).

- Andrews, S. M., Hughes, A. M., Wilner, D. J., & Qi, C. 2008, *ApJL*, 678, L133
- Andrews, S. M., Huang, J., Pérez, L. M., et al. 2018, *ApJL*, 869, L41
- Andrews, S. M., Elder, W., Zhang, S., et al. 2021, *ApJ*, 916, 51
- Astropy Collaboration, Robitaille, T. P., Tollerud, E. J., et al. 2013, *A&A*, 558, A33
- Astropy Collaboration, Price-Whelan, A. M., Sipőcz, B. M., et al. 2018, *AJ*, 156, 123
- Avenhaus, H., Quanz, S. P., Garufi, A., et al. 2018, *ApJ*, 863, 44
- Bae, J., & Zhu, Z. 2018a, *ApJ*, 859, 118
- . 2018b, *ApJ*, 859, 119
- Bae, J., Teague, R., Andrews, S. M., et al. 2022, arXiv e-prints, arXiv:2207.05923
- Ballabio, G., Nealon, R., Alexander, R. D., et al. 2021, *MNRAS*, 504, 888
- Benisty, M., Juhász, A., Facchini, S., et al. 2018, *A&A*, 619, A171
- Bohn, A. J., Benisty, M., Perraut, K., et al. 2022, *A&A*, 658, A183
- Bollati, F., Lodato, G., Price, D. J., & Pinte, C. 2021, *MNRAS*, 504, 5444
- Calcino, J., Hilder, T., Price, D. J., et al. 2022, *ApJL*, 929, L25
- Casassus, S., Cárcamo, M., Hales, A., Weber, P., & Dent, B. 2022, *ApJL*, 933, L4
- Casassus, S., & Pérez, S. 2019, *ApJL*, 883, L41
- Casassus, S., Christiaens, V., Cárcamo, M., et al. 2021, *MNRAS*, 507, 3789
- Chiang, E. I., & Goldreich, P. 1997, *ApJ*, 490, 368
- Disk Dynamics Collaboration, Armitage, P. J., Bae, J., et al. 2020, arXiv e-prints, arXiv:2009.04345
- Dong, R., & Fung, J. 2017, *ApJ*, 835, 38
- Dong, R., Hall, C., Rice, K., & Chiang, E. 2015, *ApJL*, 812, L32
- Dullemond, C. P., Dominik, C., & Natta, A. 2001, *ApJ*, 560, 957
- Dullemond, C. P., Birnstiel, T., Huang, J., et al. 2018, *ApJL*, 869, L46
- Fairbairn, C. W., & Rafikov, R. R. 2022, arXiv e-prints, arXiv:2207.14637
- Fung, J., & Dong, R. 2015, *ApJL*, 815, L21
- Gaia Collaboration, Prusti, T., de Bruijne, J. H. J., et al. 2016, *A&A*, 595, A1
- Gaia Collaboration, Vallenari, A., Brown, A. G. A., et al. 2022, arXiv e-prints, arXiv:2208.00211
- Garufi, A., Avenhaus, H., Pérez, S., et al. 2020, *A&A*, 633, A82
- Garufi, A., Dominik, C., Ginski, C., et al. 2022, *A&A*, 658, A137
- Ginski, C., Stolker, T., Pinilla, P., et al. 2016, *A&A*, 595, A112
- Goldreich, P., & Tremaine, S. 1979, *ApJ*, 233, 857
- Goodman, J., & Rafikov, R. R. 2001, *ApJ*, 552, 793
- Hall, C., Dong, R., Rice, K., et al. 2019, *ApJ*, 871, 228
- Harris, C. R., Millman, K. J., van der Walt, S. J., et al. 2020, *Nature*, 585, 357
- Huang, J., Andrews, S. M., Cleeves, L. I., et al. 2018a, *ApJ*, 852, 122
- Huang, J., Andrews, S. M., Dullemond, C. P., et al. 2018b, *ApJL*, 869, L42
- Huang, J., Andrews, S. M., Pérez, L. M., et al. 2018c, *ApJL*, 869, L43

- Hunter, J. D. 2007, *Computing in Science and Engineering*, 9, 90
- Ilee, J. D., Walsh, C., Jennings, J., et al. 2022, *MNRAS*, 515, L23
- Izquierdo, A. F., Facchini, S., Rosotti, G. P., van Dishoeck, E. F., & Testi, L. 2022, *ApJ*, 928, 2
- Izquierdo, A. F., Testi, L., Facchini, S., Rosotti, G. P., & van Dishoeck, E. F. 2021, *A&A*, 650, A179
- Jennings, J., Booth, R. A., Tazzari, M., Clarke, C. J., & Rosotti, G. P. 2022a, *MNRAS*, 509, 2780
- Jennings, J., Booth, R. A., Tazzari, M., Rosotti, G. P., & Clarke, C. J. 2020, *MNRAS*, 495, 3209
- Jennings, J., Tazzari, M., Clarke, C. J., Booth, R. A., & Rosotti, G. P. 2022b, *MNRAS*, 514, 6053
- Juhász, A., & Rosotti, G. P. 2018, *MNRAS*, 474, L32
- Kanagawa, K. D., Muto, T., Tanaka, H., et al. 2016, *PASJ*, 68, 43
- Kataoka, A., Muto, T., Momose, M., et al. 2015, *ApJ*, 809, 78
- Law, C. J., Teague, R., Loomis, R. A., et al. 2021, *ApJS*, 257, 4
- Lodato, G., Dipierro, G., Ragusa, E., et al. 2019, *MNRAS*, 486, 453
- Meru, F., Juhász, A., Ilee, J. D., et al. 2017, *ApJL*, 839, L24
- Miranda, R., & Rafikov, R. R. 2020, *ApJ*, 892, 65
- Monnier, J. D., Harries, T. J., Aarnio, A., et al. 2017, *ApJ*, 838, 20
- Muro-Arena, G. A., Dominik, C., Waters, L. B. F. M., et al. 2018, *A&A*, 614, A24
- Muto, T., Grady, C. A., Hashimoto, J., et al. 2012, *ApJL*, 748, L22
- Nayakshin, S., Tsukagoshi, T., Hall, C., et al. 2020, *MNRAS*, 495, 285
- Norfolk, B. J., Pinte, C., Calcino, J., et al. 2022, arXiv e-prints, arXiv:2208.02542
- Paneque-Carreño, T., Miotello, A., van Dishoeck, E. F., et al. 2022, arXiv e-prints, arXiv:2210.01130
- Paneque-Carreño, T., Pérez, L. M., Benisty, M., et al. 2021, *ApJ*, 914, 88
- Pavlyuchenkov, Y., Akimkin, V., Wiebe, D., & Vorobyov, E. 2019, *MNRAS*, 486, 3907
- Pérez, L. M., Carpenter, J. M., Andrews, S. M., et al. 2016, *Science*, 353, 1519
- Pérez, L. M., Benisty, M., Andrews, S. M., et al. 2018, *ApJL*, 869, L50
- Pérez, S., Casassus, S., Hales, A., et al. 2020, *ApJL*, 889, L24
- Pinte, C., Teague, R., Flaherty, K., et al. 2022, arXiv e-prints, arXiv:2203.09528
- Pinte, C., Price, D. J., Ménard, F., et al. 2018a, *ApJL*, 860, L13
- Pinte, C., Ménard, F., Duchêne, G., et al. 2018b, *A&A*, 609, A47
- Pinte, C., van der Plas, G., Ménard, F., et al. 2019, *Nature Astronomy*, 3, 1109
- Pinte, C., Price, D. J., Ménard, F., et al. 2020, *ApJL*, 890, L9
- Rabago, I., & Zhu, Z. 2021, *MNRAS*, 502, 5325
- Rafikov, R. R. 2002, *ApJ*, 569, 997
- Rosotti, G. P., Benisty, M., Juhász, A., et al. 2020, *MNRAS*, 491, 1335
- Rowther, S., Nealon, R., & Meru, F. 2022, *MNRAS*, arXiv:2210.17454
- Speedie, J., Booth, R. A., & Dong, R. 2022, *ApJ*, 930, 40
- Sturm, J. A., Rosotti, G. P., & Dominik, C. 2020, *A&A*, 643, A92
- Teague, R. 2019a, *The Journal of Open Source Software*, 4, 1220
- . 2019b, *The Journal of Open Source Software*, 4, 1632
- Teague, R., Law, C., Huang, J., & Meng, F. 2021a, *The Journal of Open Source Software*, 6, 3827
- Teague, R., Bae, J., Aikawa, Y., et al. 2021b, *ApJS*, 257, 18
- Teague, R., Bae, J., Andrews, S. M., et al. 2022, arXiv e-prints, arXiv:2208.04837
- The pandas development team. 2020, doi:10.5281/zenodo.3509134. <https://doi.org/10.5281/zenodo.3509134>
- Tomida, K., Machida, M. N., Hosokawa, T., Sakurai, Y., & Lin, C. H. 2017, *ApJL*, 835, L11
- van der Velden, E. 2020, *The Journal of Open Source Software*, 5, 2004
- Verrios, H. J., Price, D. J., Pinte, C., Hilder, T., & Calcino, J. 2022, arXiv e-prints, arXiv:2207.02869
- Virtanen, P., Gommers, R., Oliphant, T. E., et al. 2020, *Nature Methods*, 17, 261
- Zhang, S., & Zhu, Z. 2020, *MNRAS*, 493, 2287
- Zhang, S., Zhu, Z., Huang, J., et al. 2018, *ApJL*, 869, L47
- Zhu, Z., Dong, R., Stone, J. M., & Rafikov, R. R. 2015, *ApJ*, 813, 88
- Zhu, Z., & Zhang, R. M. 2022, *MNRAS*, 510, 3986